

Innovations on In-Situ Processes for Production of Aluminum-Matrix
Nanocomposites

by

Jeremy Fedors

WORCESTER POLYTECHNIC INSTITUTE

in partial fulfillment of the requirements for the

Degree of Master of Science

in

Materials Science and Engineering

December 2018

Dr. Brajendra Mishra, Major Advisor

Dr. Richard Sisson, Director of Manufacturing and Materials Engineering

Abstract

Increasing the mechanical properties of cast aluminum components at temperatures in the vicinity of 300°C will allow for lightweighting opportunities, especially in automotive and aerospace applications. Metal-matrix nanocomposites show great promise in this regard, in the form of aluminum as a matrix containing well-dispersed ceramic nanoparticles. These have been shown to retain most of the ductility of the matrix alloy, while adding strength and stiffness at far lower reinforcement fractions than are required in microcomposites. Unfortunately, metal-matrix nanocomposites are plagued by issues which limit commercialization, such as high costs of production, issues with particle wetting and dispersion, low potential for scalability and poor castability. In this work, two existing metal-matrix nanocomposite manufacturing processes showing promise to overcome some of these obstacles were developed further: the in-situ gas-liquid reaction, and self-propagating high-temperature synthesis. Composites reinforced with aluminum nitride and titanium carbide were produced, alloyed with several matrix compositions and squeeze cast. Insights into the effects of process design on microstructure and properties were gained, and potential process improvements and areas to focus future research were identified.

Acknowledgements

To my advisor Brajendra Mishra, and professors Danielle Cote, Diran Apelian and Richard Sisson, for being sources of inspiration as I dove into the world of materials science as well as being respectful and accommodating as I passed through an undesirable phase on my way to equilibrium.

To Fellow members of this collaborative project, including David Weiss, Steve Udvardy, Alan Taub, and his UM team, who supported the work at WPI as we faced unforeseen obstacles and setbacks.

To Inigo Anza and Eunkyung Lee for contributing invaluable knowledge and hands-on experience in the earlier stages of the project.

To other colleagues who added spice to my time at WPI, including Renee Brodeur, Audrey Jean-Philippe, Alino Te, Qiang Wang, Sumedh Gostu, and Carl Soderhjelm.

To our MPI and Materials Science staff and especially lab manager Michael Collins and procurement assistant Meagan McIntosh.

To Reverend Cheryl Leshay for her thoughtful spiritual guidance.

To my loving support crew in Maryland and especially my parents for their constant support and encouragement.

Table of Contents

1	Introduction	4
1.1	Motivation	4
1.2	Objectives	4
1.3	Literature review.....	5
1.3.1	Existing elevated temperature alloys	5
1.3.2	Overview of Al-MMNC manufacturing processes	6
1.3.3	Taking advantage of the strengthening potential of in-situ Al-MMNCs	10
1.3.4	ISGR: background.....	11
1.3.5	SHS: background	15
2	Experimental Methods.....	18
2.1	Experimental overview	18
2.2	ISGR approach	19
2.2.1	Small-scale system.....	19
2.2.2	Scaled-up system.....	22
2.2.3	Glycerin/water fluid model	28
2.3	SHS approach	29
2.3.1	General process	29
2.3.2	Experiments	31
3	Results and Discussion	36
3.1	ISGR	36
3.1.1	Small-scale system.....	36
3.1.2	Large-scale system.....	37
3.1.3	Glycerin/water fluid model	42
3.1.4	Discussion	46
3.2	SHS	48
3.2.1	Results.....	48
3.2.2	Discussion	61
4	Recommendations for future work	64
4.1	ISGR	64
4.2	SHS	65
5	References	66

1 Introduction

1.1 Motivation

The ability to produce lightweight and economical cast aluminum components which can maintain high strength and stiffness in or above the 230-300°C temperature range is desirable for a variety of applications. This is especially valuable in many aerospace and ground transportation components. Aluminum is desirable because of its low density and high ductility, though currently almost all aluminum alloys have a severe drop-off in strength and stiffness in this temperature range. Aluminum with significantly increased strength could replace steel components or could maintain the integrity of currently-used aluminum components while using less material. In the case of internal combustion engines, a thinner-profile aluminum piston could improve the combustion efficiency of the engine,¹ and other components such as cylinder heads could be made stronger and/or lighter as well.

Discontinuously-reinforced aluminum metal-matrix nanocomposites (Al-MMNCs) hold great promise to fulfill this need. These consist of a continuous matrix containing one or more types of ceramic nanoparticle reinforcement phase, with the particles being formed either outside the matrix (ex-situ) or inside (in-situ). Though high-performing MMNCs have been successfully produced at the lab scale and for niche applications, attempts to scale up processes economically have been met with serious challenges. Advancing the most promising processes as well as gaining a better understanding of Al-MMNC properties at various temperature and loading conditions will be of great benefit in the continuing push towards lighter and higher-performing materials.

1.2 Objectives

Produce nanocomposite master alloys

In-situ MMNC processes, as will be explained later, have advantages which make them appealing for being considered for commercialization. Therefore, this work aimed to innovate on two promising in-situ processes, the in-situ gas-liquid reaction (ISGR) and self-propagating high-temperature synthesis (SHS), with the goal of large-scale production in mind. Several types of reinforcements can be made using ISGR and SHS, but specifically aluminum-aluminum nitride (Al-AlN) and aluminum-titanium carbide (Al-TiC) reinforcements, respectively, would be the

focus as they are relatively easy to synthesize. These composites would be first produced in a molten state in concentrated form, as master alloys which could be further processed for casting.

Dilute master alloys and produce castings

For materials showing a favorable microstructure, the aim was to dilute them to ~2 volume percent (vol%) reinforcement levels in a casting alloy, in order to produce test pieces firstly via squeeze casting and secondly via high-pressure die casting. Alloys primarily containing Al and Si, such as A356, were preferred due excellent castability.

Verify room-temperature and elevated temperature properties

To ensure that squeeze-cast material was viable, tensile bars cut from test plates would be tested, and hardness measured. If the results were favorable, tests would also be run at 300°C.

Demonstrate die casting of composites and develop heat treatment

Work did not progress to this stage, but material that could also perform well in die casting is the ultimate goal for these types of composites. A heat treatment needs to be created and optimized for the service temperature, so for A356 or other precipitation-strengthening alloys as the matrix, a more stable over-aged treatment may be appropriate. Once a heat treatment is developed, squeeze and die casting of more complex shapes can proceed.

1.3 Literature review

Numerous approaches have been taken with the goal of producing aluminum-based materials which can perform well at elevated temperatures. The following sections will briefly explain some of the alternative approaches to this problem, explain why nanocomposites and specifically in-situ methods are appealing, and present the background of the ISGR and SHS processes.

1.3.1 Existing elevated temperature alloys

Some non-nanocomposite Al alloys have been designed for elevated temperatures around the same range in which low-fraction MMNC's would likely be applied. Several near-eutectic aluminum-magnesium-cerium (Al-Mg-Ce) alloys have been developed at Eck Industries, Inc., one of which

has shown castability similar to 300-series alloys, while demonstrating high strength at up to 260°C. These alloys contain fine lath eutectic structure which does not coarsen at elevated temperatures due to the lack of solubility of cerium in Al.²

Another innovative approach is the series of Al-Si alloys developed by NASA, which derive their strength from eutectic and primary silicon precipitates which are stabilized by the addition of strontium and phosphorous³. These have shown impressive tensile strength tested at up to 371°C, at which the tensile strength was 2-3x that of several alloys for engine piston applications.¹ However, a disadvantage of these alloys is that they are more difficult to cast than the cerium alloys.⁴

These and other alloys utilizing high temperature-stable precipitates could prove to be more economical for some cast components versus MMNC's, though it remains to be seen if well-developed commercial MMNC's can add additional strength and stiffness which can be maintained at the same or higher temperatures than these alloys. Depending on the compatibility of reinforcement and matrix, nanoparticle strengthening could someday be integrated into one of these alloys for maximum benefit.

1.3.2 Overview of Al-MMNC manufacturing processes

Al-MMNC development is a lively field, and the list of production techniques currently being applied is too long to discuss in much detail here. To put this work in context though, some categories and processes are important to note. Some of these have been shown to produce composites with impressive properties but require time-consuming and expensive processing steps to produce small amounts of material and are not easily scalable. A primary challenge for large-scale casting of MMNC's is to minimize time, energy and expensive feedstock needed for production in order to maximize the number of applications for which they are economical solutions.

Depending on the process, some composites will have high percentages of reinforcement phase, for example up to 30vol% in SHS material,⁵ making their properties closer to that of the pure ceramic. For high compressive strength, stiffness and wear resistance, this can be desirable. To

expand the applications of these materials to a greater variety of cast components though, MMNC's which maintain most of the ductility of the metal matrix as well as relatively low viscosity and other good casting properties need to be developed.

A few of the more common Al-MMNC processes are listed in Figure 1. The processes are grouped based on whether reinforcements are integrated into a liquid or solid matrix, and whether the reinforcements are produced outside (ex-situ) or inside (in-situ) the matrix material.

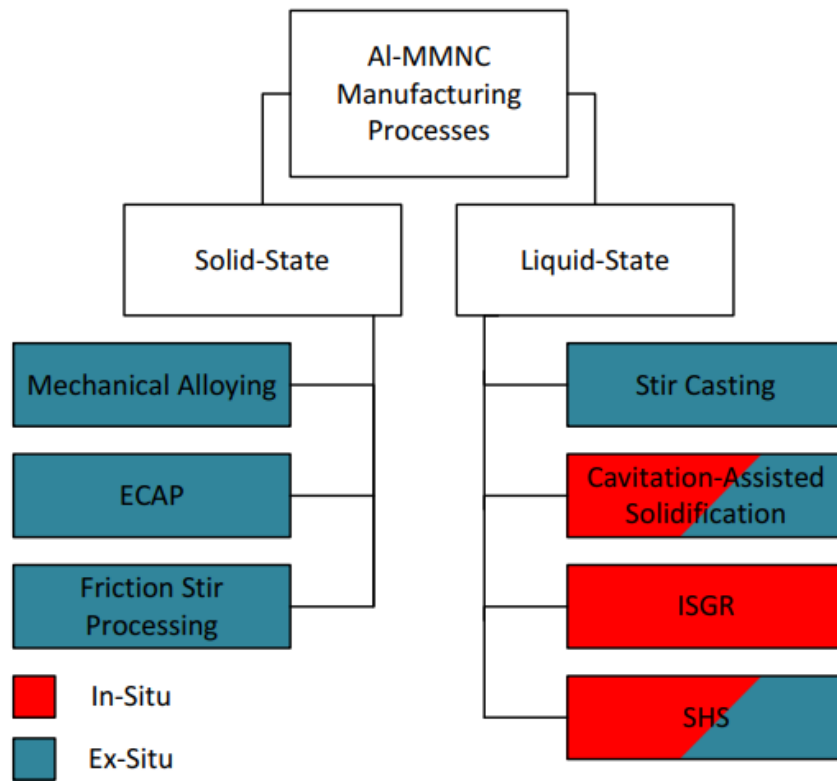


Figure 1: Several examples of Al-MMNC manufacturing processes

Solid-state processes

Mechanical alloying is a type of powder metallurgy process in which high-energy ball milling is used not only to blend powders but also for size reduction (attrition).⁶ The resulting powders can be cold or hot pressed and sintered before further processing, such as extrusion. Milling can reduce agglomeration of particles and lead to high strength through grain size reduction and lattice strains. Mechanical alloying has been used successfully to produce nanocomposites such as the Al-

aluminum carbide (Al_4C_3) DISPAL, though limitations include the high energy needed to produce composites as well as the risk of contamination by the milling tool and atmosphere.⁷

Equal-channel angular pressing (ECAP), where the material is subjected to intense plastic strain by being pressed through an angled channel, producing ultrafine grain materials without changing the overall dimensions.⁸ It has been applied to the manufacture of both fiber and particle-reinforced Al-MMNCs and may be a promising process, though scale-up could be an issue.⁷

Friction-stir processing also relies on severe plastic deformation, though in this case a rotating tool contacts the material to heat and deform it. It is typically used as a solid-state welding process, though it has also been applied to make Al-MMNCs by stirring silicon carbide (SiC) powder into the matrix. The major downside of friction-stir processing is that it can locally reinforce materials, but is not favorable for production of bulk MMNCs.⁷

Liquid-state processes

Stir casting consists of using mechanical stirring to distribute reinforcements in the melt and has been most successfully used for microcomposites. When attempting to stir nanoparticles into a melt, the high surface energy causes particle agglomeration as well as bond strength possibly decreasing due to surface contamination.⁷ Xiaodan et al. were successful in producing stir-cast Al-SiC composite using an impeller-stirred vacuum melting system, though it was limited to 0.5 weight percent (wt%) SiC for good dispersion.⁹

Cavitation-assisted solidification involves applying ultrasonic energy to the melt before or during casting in order to integrate nanoparticles into the matrix. It has been applied in numerous studies both using a sonotrode directly in the melt^{10,11} as well as applying the ultrasonic energy to the mold during casting¹². Ex-situ produced nanoparticles resist passing through the oxide layer of an Al melt surface, but processing is aided by using a salt flux to break down the layer and encourage the particles to wet the liquid.¹¹ Processing variations can be used to aid processing of in-situ composites as well, including in this work.

ISGR is a process by which a reactive gas is inserted into a melt to form reinforcement particles, and in the case of nanocomposite production it requires vigorous stirring of the melt. It has been applied successfully to produce AlN using nitrogen-bearing gases in Al-Li and Al-Mg melts, as well as TiC using carbon-bearing gases in Al-Ti. It has the advantages of low consumable material costs as well as being promising in terms of scalability.¹³ A primary obstacle to commercialization is that process control to produce high fractions of homogeneous nanocomposite is challenging.

SHS, also known as combustion synthesis, was originally developed as a technique to manufacture a wide variety of ceramic materials and intermetallics. Traditionally, it is a process in which a cylindrical powder pellet is ignited at one end, starting a highly exothermic reaction which heats the remaining reactants to allow the combustion wave to propagate to completion.¹⁴ It has recently been adapted to the production of Al-MMNC's reinforced by Al-TiC, Al-TiB₂, and others. This can be done using the traditional ignition method, after which the products are dispersed into an Al melt (ex-situ), or by reacting the powder compact directly in the melt (in-situ).^{15,16} Though the cost of powders gives it a disadvantage relative to ISGR, a wider variety of reinforcements are possible and simpler equipment is required.

Some of these processes, especially SHS, have resulted in particles in the range below one micron but greater than 100nm. 100nm is often used as the definition of nanoscale, and applying this to nanocomposites Zhang and Chen have claimed this as a "critical size for nanoparticulate-reinforced MMNCs to produce excellent mechanical properties...¹⁷" It remains to be seen if a single critical size can be assumed for all particle-reinforced MMNCs, but there has not been as much research into composites in the grey area above 100nm, which could be called metal-matrix submicrocomposites (MMSCs). It is possible some of these will be useful as a compromise between the expense and difficulty of processing smaller nanocomposites and the limited properties of microcomposites.

1.3.3 Taking advantage of the strengthening potential of in-situ Al-MMNCs

Strengthening mechanisms

Several strengthening mechanisms can occur as a result of the addition of reinforcement particles to Al. Yang et al report that Orowan strengthening, load-bearing effect of the particle-matrix interface, and strengthening due to thermal mismatch are all important to consider in MMNCs¹⁸. Yield strengths of MMNCs also increase due to the Hall-Petch relationship, as a result of grain refinement.¹⁹

Orowan strengthening results when dislocations moving under applied stress encounter hard reinforcement particles which cause the dislocation to bow between them and create loops, if the particles are too hard to be sheared⁷. In nanocomposite materials, there is evidence that this is a significant source of yield strength for reinforcements which are below 500nm, but particles around 1 μ m and larger have interparticle spacing which is too large to noticeably impede dislocations.⁶ This mechanism is likely synergistic with quench strengthening, and is only expected to apply when particles are incorporated into grains.¹⁷ Yang et al proposed an analytical model to predict the nanoparticle strengthening from this effect, which has some experimental support.¹⁸

Quench strengthening arises from the difference in thermal expansion coefficient (Δ CTE) between reinforcement and matrix. Once particles are incorporated into the matrix and the material cooled, this causes plastic deformation and geometrically necessary dislocations (GND's) which result in higher yield strength²⁰.

Clearly the interface between particle and matrix is critical, and TiC is promising in this regard. It has been widely used in nanocomposites and can also be used as a grain refiner for Al, providing an excellent surface for Al grains to nucleate on and form an excellent bond.¹⁸ Al-AlN composites have not been studied to the extent of Al-TiC since AlN is not generally used in ex-situ methods, but there is at least evidence for macro-scale interfaces between Al-AlN having stable and high-strength bonds at high temperatures.²¹ Particle size could affect the bond for either material, and the proliferation of in-situ MMNCs and MMSCs will allow for further study of the interfaces between various matrix-particle combinations.

Particle dispersion

Due to the desire for composites to benefit from Orowan strengthening as well as the generally-accepted fact that clustered particles tend to reduce ductility, materials and processes need to be optimized to ensure particle dispersion and engulfment in grains. For liquid-state MMNCs, there are two stages at which particles can become clustered: during introduction of reinforcements into the melt, and during solidification. Ultrasonic cavitation has been demonstrated as a good method of solving the former problem. The extreme temperatures and pressures produced during cavitation, up to 5000°C and 1000atm for a few nanoseconds, tend to disperse nanoparticle clusters and clean their surfaces to encourage wetting.¹⁰

During solidification, particles can cluster in interdendritic spaces and grain boundaries if they are pushed by the solidification front instead of engulfed into grains. A few different models have been developed to predict the interaction between micro- or nanoparticles and a solidification front. Xu et al explained that presently, accurate predictions can generally not be made for nanoparticles until more experimental work is done. They presented a model which accounts for the balance of interfacial energy, Brownian motion energy, net interaction energy and Van der Waals potential which can result in either spontaneous capture of particles or an energy barrier which pushes the nanoparticle against viscous drag in the liquid²².

1.3.4 ISGR: background

1.3.4.1 Previous development of the Al-AlN and Al-TiC production processes

Al-AlN Process

The origin of what could be called an ISGR composite production process was in the form of nitridation reactions on an Al surface. In a process known as PRIMEX, composites are synthesized by melting Al alloys under a highly pure nitrogen or nitrogen-hydrogen mix atmosphere. This results in a composite containing a high volume fraction continuous AlN reinforcement.²³ Knowledge gained from this early work contributed to the possibility of producing MMNC's. Importantly, nitridation was found to happen slowly unless a highly reactive alloying elements such as magnesium, lithium, or sodium was present, and silicon tends to slow the reaction.²⁴

More recently, Borgonovo and Makhlof explored nitridation by bubbling high-purity nitrogen or ammonia into an Al alloy melt.^{7,25,26} This process was successful in producing AlN microparticles at 1000°C, in an Al-Mg or Al-Li melt. The reaction using Al-Li was faster, while using a much lower percentage of alloying element vs Mg. A version of the process in which a ceramic pitched blade downflow (PTD) impeller stirred the melt during gas insertion was then developed, which reduced the particle size. A schematic of this process is shown in Figure 2. In rotary experiments, nitrogen, ammonia, and ammonia-nitrogen mix were all attempted. Ammonia was found to speed up the reaction process, though it proved difficult to control the reaction, leading to high fractions of microparticles. Experiments which produced the most AlN as nanoparticles used Al-Li alloy at 1050°C, reacted from nitrogen. After dispersing this material in A356, ultrasonic processing was applied, followed by squeeze casting. The most high-performing material contained 1vol% AlN, and showed an almost 50% tensile strength increase versus A356 at 300°C.⁷

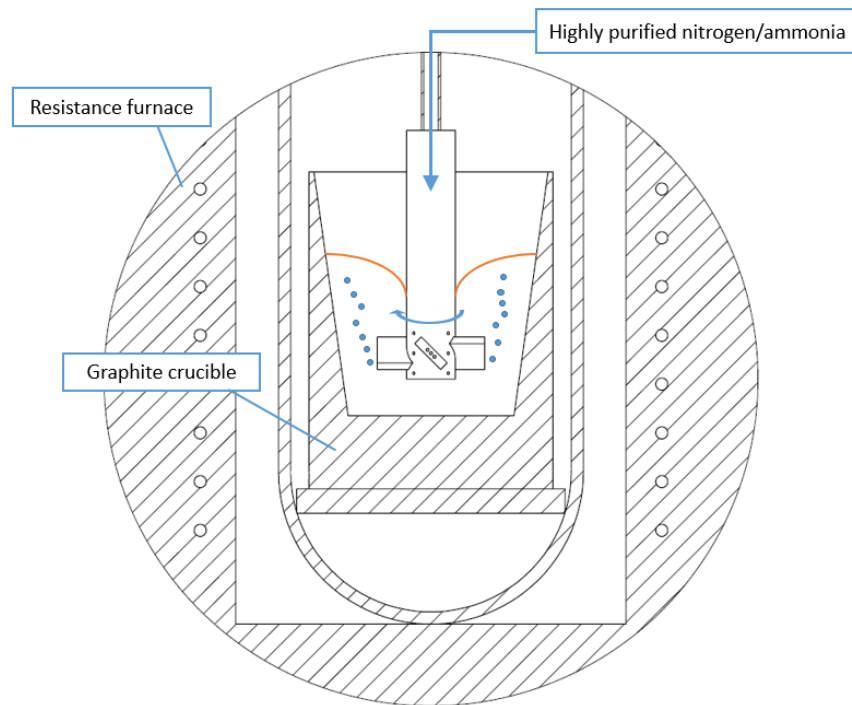
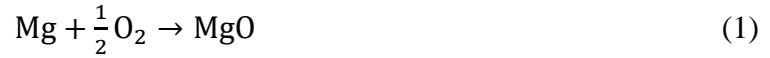
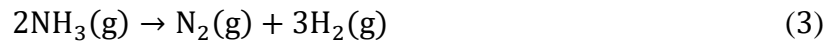


Figure 2: Schematic view of the rotating impeller ISGR process for production of AlN nanoparticles

Borgonovo and Makhlouf proposed a reaction mechanism which explains the necessity of either alloying elements or ammonia to facilitate the AlN reaction.²⁶ In the case of nitrogen at 1000°C, aluminum oxide will form preferentially to AlN unless the partial pressure is below $5 * 10^{-20}$ psi, which is not likely even with highly-purified gas. However, volatilized Mg or Li in the bubbles act as oxygen getters, clearing oxygen from the gas-liquid interface:



In the case of ammonia, alloying elements are not required, since the ammonia molecules dissociate and hydrogen acts as the oxygen getter:



This allows nitrogen chemisorption and mass transfer into a dissolved gas boundary layer in the melt, followed by the formation of AlN:



A two-film model, which is typically used for gas-liquid interactions in bubble column reactors, is assumed to describe this reaction.²⁶

Al-TiC process

Anza and Makhlouf adapted the process to produce TiC from an Al-Ti melt.^{27,28} The process hardware was similar to that of the Al-AlN process, although the impeller modified and with the nitrogen and ammonia replaced by argon-diluted methane or other carbon-bearing gas. This process proved to be challenging especially in terms of reducing soot production, which is necessary to prevent microparticles from forming. Material containing a small fraction of nanoparticles was produced after the fluid flow pattern was modified by adding baffles to the crucible in a similar way to a traditional chemical mixing tank.²⁷ The theory and process developed

through their work paved a path for possible high-performing material in the future, though the Al-TiC process is further from commercialization. Therefore, only the Al-AlN process was attempted in this work.

1.3.4.2 Mixing and gas dispersion considerations

The results of the Al-AlN process indicate that a sufficient impeller velocity is critical for producing AlN in the nanoscale range. At 250RPM using only nitrogen, AlN only formed in an Al-5wt%Li melt with particles an average of 643nm. At 450RPM, particles with an average size of 58nm formed in a melt with only 2.5wt%Li.²⁵ In order to optimize this process with the eventual goal of improved properties and economics for commercialization, it is necessary to produce optimum mixing characteristics, gas flow etc. to produce the maximum number of particles in the minimum time, while avoiding excessive particle growth.

In the Al-TiC process, the impeller rotated at 450 RPM for all experiments, but nanoparticles did not form noticeably in until baffles were added, extending from the crucible walls²⁸. In many industrial mixing applications, baffles are added in the form of usually 2-4 vertical plates spaced slightly away from the tank wall. These increase the power delivered to mixing and gas dispersion for a given RPM, as well as and encourage vertical recirculation.²⁹ The comparison of these arrangements is shown in Figure 3. Baffles are an especially good addition when it comes to scaling up the process, since they prevent the in terms of increasing bubble interfacial area and preventing the swirl and vortex flow which tends to be more pronounced in larger vessels, and the added shear can increase bubble interfacial area to increase the reaction rate.³⁰

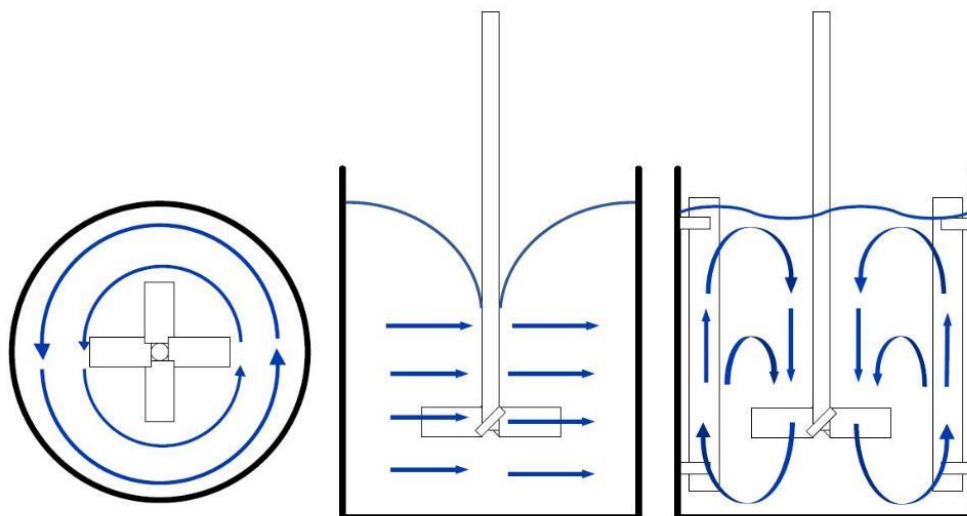


Figure 3: typical flow patterns for un baffled and baffled mixing tanks stirred using a PTD impeller.

Typically, when developing or scaling up mixing processes, empirical correlations are used to relate dimensionless numbers, geometric ratios, mass flow rates etc. in order to make design decisions. However, these tend to only be accurate for the standard mixing tanks and impellers used for the particular correlation, and correlations which account for a third phase are even more difficult to come by.²⁹ As an example of this difficulty, Anza provided a calculation for the necessary impeller RPM to wash TiC particles from the surface of a bubble in order to prevent them from remaining in the boundary layer of the bubble and growing past nanocale²⁸. This derives from the energy dissipation rate of the impeller, taken from a mixing tank correlation.³¹ However, this correlation was for a different impeller and mixing tank geometry, and did not fit well with the ISGR experimental results. Development of correlations specifically for the ISGR process could be required in order to reasonably predict this RPM or related dimensionless numbers, as well as allow prediction of the reaction rate.

1.3.5 SHS: background

A schematic comparison of the two versions of the SHS process is shown in Figure 4. In the traditional ex-situ self-propagating reaction, the reactants are ignited at one end and the reaction proceeds linearly. The reaction is simple to ignite, though it requires the use of a vacuum or inert atmosphere chamber in order to avoid oxidation of the outer surface. In the in-situ reaction, the

reactant pellet is preheated by the melt, removing a step in the process as well as the requirement of a protected atmosphere. It is possible for all reactants to reach ignition temperature simultaneously (explosion mode) or in a nearly-explosion self-propagating reaction.

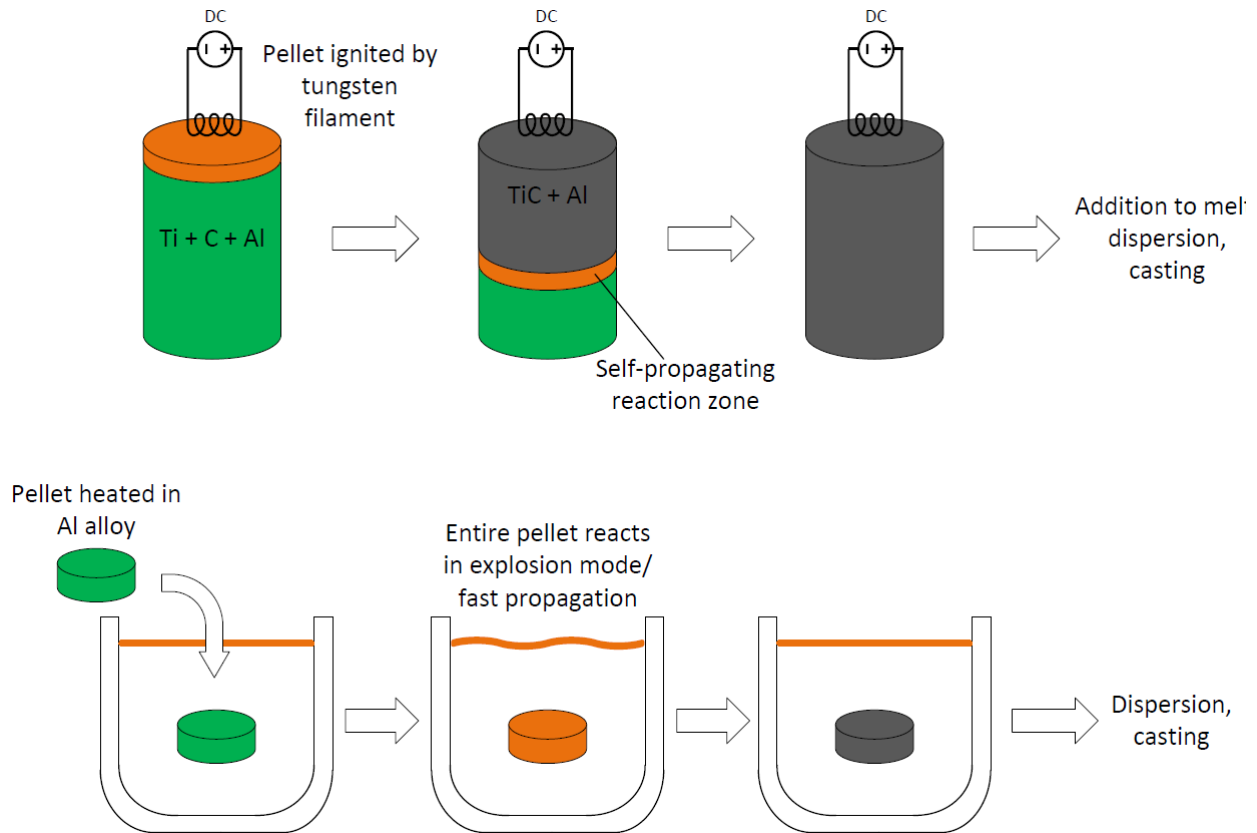


Figure 4: comparison of the in-situ and ex-situ SHS processes for MMNC production.

Extensive work has been done, especially at the Colorado School of Mines, towards applying these methods to producing micro- and nanocomposites. Garrett studied primarily the ex-situ reaction for production of TiC, including measuring SHS reaction temperatures to determine the change in combustion temperature resulting from diluents being added to the powder mix. Dilution of the Ti-carbon mix with Al or TiC resulted in a lower resultant TiC particle size, and Al was especially good for particle size reduction. Over 30wt% Al resulted in the molten spaces between reactants being large enough that TiC particles grew without influence of each other.³²

Work on SHS by Garrett included 10-30% TiC in composites, produced ex-situ and later integrated into melts. Composites were tested only at room temperature showed excellent compressive strength, but tensile strength not much greater than the matrix as well as poor ductility. The material was targeted mainly for use in military armor as well as cast iron replacement, where compressive strength is a primary concern.³²

Cho et al. produced MMNCs using an in-situ process, using Al-Ti-C powders as well as a formulation with the addition of cupric oxide (CuO). Based on cross-sections of pellets, they observed Al₃Ti as well as carbon along with the TiC in some partially-reacted zones, and proposed the following reaction mechanism:¹⁵

During the preheating stage, Al and Ti first react, likely while the reactants are solid as well as liquid:



For pellets containing CuO, a thermite reaction provides the heat needed to quickly activate the remainder of the SHS reaction:



The temperature increases further, while reaction of equation 6 continues with liquid Al, until dissolution occurs:



Then, if the temperature is above 1281°C, it is more thermodynamically preferable for the TiC to nucleate from dissolved reactants:



whereas below 1281°C, it is more likely that the dissolved Ti will react with solid carbon. Their work also progressed towards determining the maximum size of Ti and C which will result in a complete reaction, as a function of initial melt temperature.¹⁵ Compared to plain matrix alloys of

similar composition, TiC-reinforced material with an average particle size (APS) of 0.74 μ m showed slight increases in strength at room temperature. Hardness was tested at 300°C and 350°C, with the reinforced material maintaining higher hardness than the plain matrix over an extended period of time. However, the material had some issues with particle clustering, and percent elongation decreased from 5.9% to 1.3% when the TiC fraction was increased from 6-12%.²⁰

Nuechterlein et al. further explored ex-situ as well as some in-situ experiments. A particularly interesting development from his work was the use of more complex reaction chemistries including the TiO₂-based reaction in equation 12, in which particles were produced via the ex-situ route.^{16,33}



After dispersing in Al-4.5%Mg, particle size was reported between 50-500nm, with improved tensile and yield strength versus the matrix alone, though severely decreased ductility.¹⁶ This and similar chemistries using alumina to reduce the reaction temperature may be promising because of the evidence of reduced TiC particle size, but the alumina resists wetting the matrix after being produced ex-situ.³³ Ductility of Al-TiC composites is also inherently higher than Al-Al₂O₃ because of the metallic bond, and the interface between Al₂O₃ could be weakened by reaction with Mg in aluminum alloys³⁴.

2 Experimental Methods

2.1 Experimental overview

The goal of this work was to innovate on both the SHS process by producing TiC-reinforced composites similar to those from Cho et al. and the research at Colorado School of Mines, as well as the Al-AlN ISGR developed at WPI. Since the earlier work on Al-AlN ISGR demonstrated promising results at 2vol% and lower, that was the proposed target for diluted material in both processes for this work. The experiments were exploratory, as the processes were iteratively modified during the sequence of experiments in order to improve the reliability and ease of manufacturing as well as the properties of the composites and with minimal use of expensive techniques.

Many of these experiments were characterized only in the master alloy state. In order to produce castable composites with low reinforcement fractions, several of them were also diluted in A356, or in the case of SHS, produced in a one-step process, simultaneously with ultrasonic processing. The device used was a Southwire Ultra-D Degasser, shown in Figure 5. It can both provide high-powered ultrasonic cavitation as well as feed inert gas through the sonotrode tip.



Figure 5: ultrasonic degasser used before casting of ISGR and SHS material, demonstrated in water.

2.2 ISGR approach

2.2.1 Small-scale system

At the start of the project, most components of the Al-AlN and Al-TiC ISGR system were available in the laboratory except that the only remaining impellers were of the type which was used for the Al-TiC process Figure 6 but not for Al-AlN. These impellers were provided to Anza and Borgonovo by collaborators who were unable to produce more for the present work. They were produced from an alumina-silica mix using powder bed additive manufacturing process, and once fully fired were 2in. in diameter at the blade tips, with gas input hole diameters close to 0.1in.

The inability to procure new 3D-printed impellers in a reasonable amount of time prevented replication of the previous Al-AlN experiments, though evaluation of the performance of the six-bladed impeller was still considered to be useful. If the six-bladed impeller performed as well or better than the four-bladed one, the design of the new impeller could be based on it. Since the system was to be redesigned with components being more practical and economical for eventual industrial use, any new impeller needed to be designed with this in mind. The hole configurations on these impellers were a concern in terms of design for manufacturing and the risk of holes being difficult to unclog.

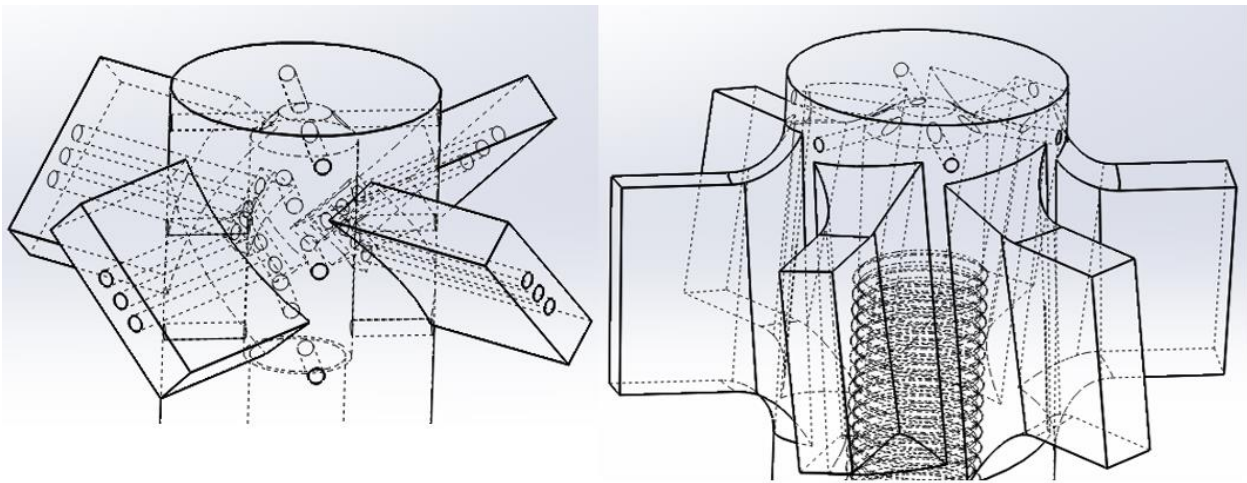


Figure 6: internal views of impeller designs used by Borgonovo (left, fillets removed for visibility) and Anza (right).

The exterior of the furnace assembly is shown in Figure 7. The drive shaft was a hollow Inconel 601 tube fed through the furnace lid and heat shield and driven by a Caframo mixing motor with a rotary gas connection for nitrogen input. The mullite retort served as a secondary containment which could be used to maintain an argon atmosphere around the crucible. Because the temperature difference between the upper and lower portions of the retort could result in cracking, the furnace heating rate was limited to 200°C/hour, along with the use of an Inconel heat shield hanging from the underside of the lid.

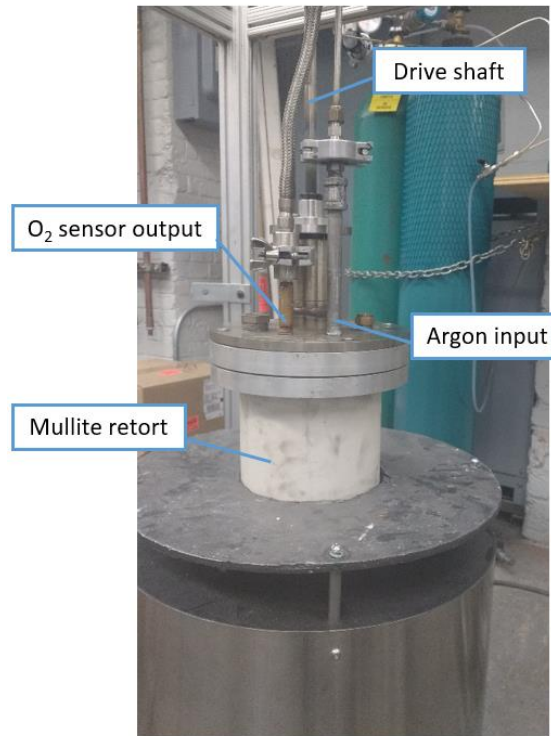


Figure 7: 2.5lbs capacity ISGR furnace.

The interior of the system was arranged in a similar way as Figure 2 from section 1.3.4.1, with the impeller cemented to the end of the drive shaft and positioned 0.75in. from the bottom of a graphite crucible. Research-grade nitrogen was used as the reactive gas, after feeding through Drierite to remove water and a three-step process to remove oxygen: a Vici high-capacity oxygen trap (Vici T300-2), an indicating oxygen trap (Restek IOT-250), as well as a tube filled with copper turnings in a secondary furnace heated to 450°C. For all experiments, the melt was stirred at 450RPM, the nitrogen flow rate was 1L/min and the temperature was kept close to 1050°C, with some variability down to a minimum of 1015°C. The crucible contained ~2.5lbs of metal, half being 99.99% pure Al and the other half Al-5%Li master alloy. The ingot needed to solidify under inert atmosphere because of the extreme reactivity of molten Al-Li, hence the slanted crucible.

Procedure in brief:

1. Place Al-Li ingots in crucible and attach lid along with rotary system and gas lines
2. Heat Al-Li alloy under argon atmosphere with <1% oxygen
3. Lower impeller into melt

4. Stir for ~5 minutes with argon flowing into melt, to ensure alloy is homogeneous
5. Flow nitrogen into melt for the desired amount of time while stirring
6. Switch gas flow back to argon, then stop stirring
7. Lift impeller out of melt, and allow the ingot to cool in the furnace
8. Remove the solid ingot from the furnace and take samples for analysis
9. Send material to be diluted and squeeze cast

Four attempts were made with this setup. experiment 1 failed as the retort fractured at the lower end, causing the crucible to fall to the bottom of the furnace. The retort fracture was possibly a result of the crucible being lowered into the support brick in the retort with too much force during setup, which could lead to later crack growth.

Experiment 2 resulted in the impeller blades breaking off into the melt, possibly due to inconsistency of the post-processing of the additive-manufactured impellers. The reaction time was reduced from 2 hours to 1.5 hours, in case the impellers were unable to handle significant particle fractions. Two more experiments were run, which went smoothly without any hardware breakage. The combined material from these experiments used in the A356 dilution stage.

2.2.2 Scaled-up system

Experiments 1 & 2

Initially, the scaled-up process used the same 12mm diam. Inconel shaft and furnace lid as the small-scale experiment. Several changes were made in order to solve the hardware issues of the small-scale version. The retort was removed, since it was a weak point which was prone to unexpected cracking. The furnace was instead sealed reasonably well, and a higher argon flow was used in order to prevent an unacceptable level of oxygen intrusion. The updated impeller, pictured in Figure 8 attached to the lid assembly, was custom cast from oxide-bonded SiC, procured from Anderman Ceramics. The high-capacity oxygen trap was replaced with one capable of a higher

flow rate (Oxiclear RGP-250-R1). The lid assembly was mounted on an adapter plate on top of a larger furnace with an insulated top, shown in Figure 9. The braces around the edge of the furnace served to keep both the furnace lid and the mixing motor, which was mounted on a wheeled cart, concentric with the crucible.

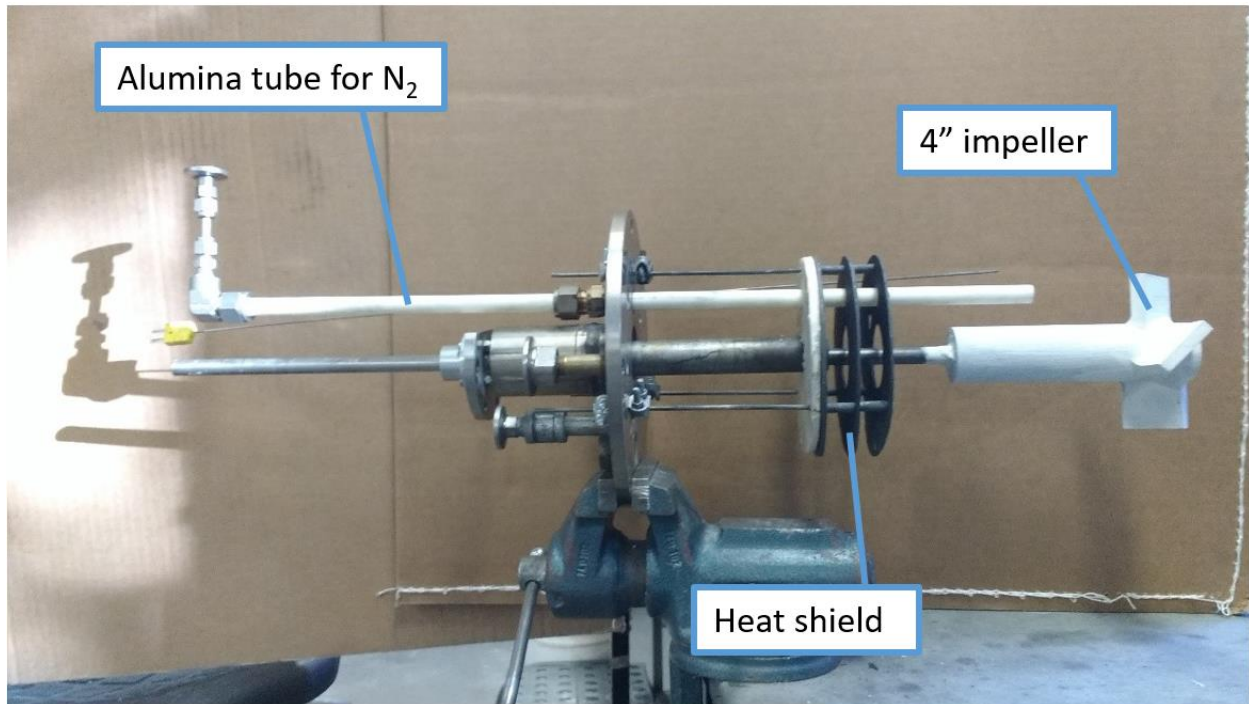


Figure 8: Lid assembly for the first scaled-up experiment

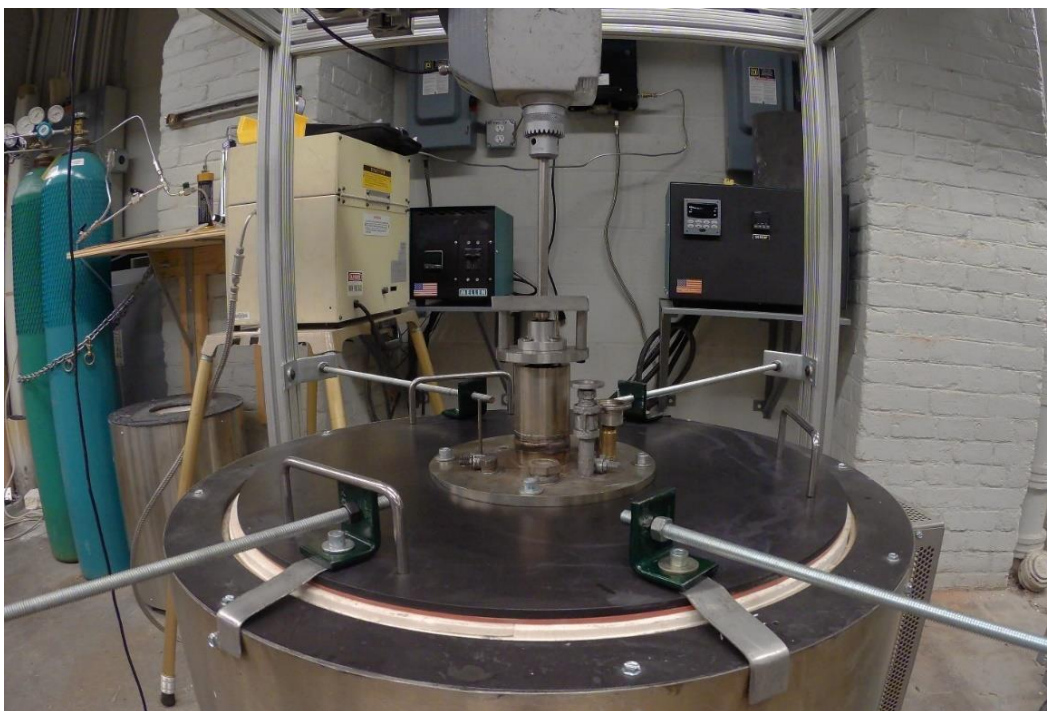


Figure 9: furnace assembly for experiments 1 and 2

Nitrogen insertion was attempted using a separate alumina furnace tube, with the intention of comparing this to gas insertion through the bottom of the impeller. The $\frac{1}{2}$ in. OD tube was locked in position using a gas line fitting with PTFE ferrules, and the nozzle at the end was a six-hole plug with hole diameters of 0.055 in. cemented flush with the tube end. The other nozzle options prepared for future experiments were a single-hole 0.133in. ID nozzle and a 0.094in. ID nozzle which also protruded ~ 0.25 in. from the end of the tube.

The crucible was machined from graphite with the dimensions in Figure 10. Unfortunately, during the experiment the crucible cracked, allowing Al leakage into the furnace chamber. This was only discovered after the experiment ended. It was thought that water in the graphite may have not been able to escape quickly enough before rupturing the crucible, as well as the possibility of the thin upper edge of the crucible heating faster than the bottom, helping to initiate cracks.

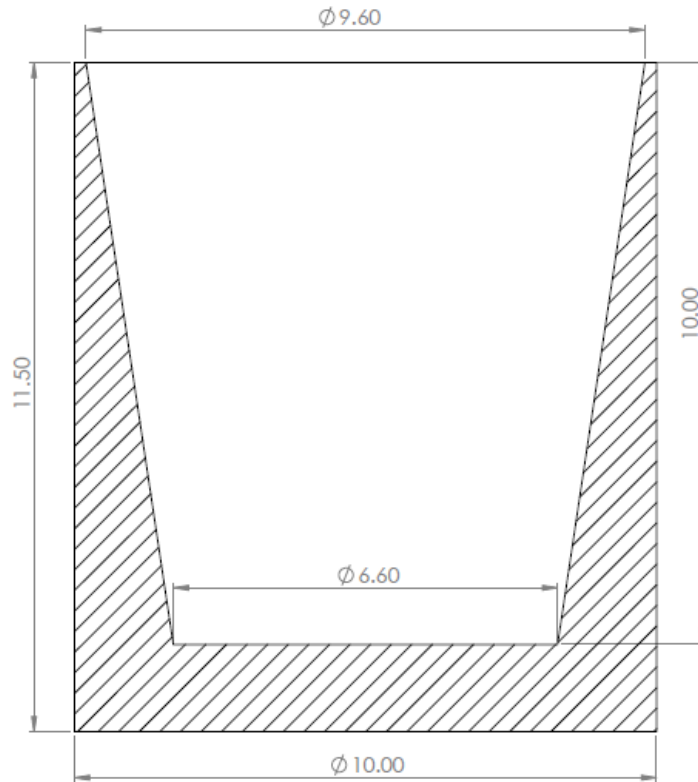


Figure 10: cross-section of failed crucible used in experiment 1, with dimensions in inches

Crucible cracking may have not been a problem for the small system, since the water was more able to escape from a crucible with a lower volume to surface area ratio. The crucible was re-designed with a 1/2in. increase in OD in case the thin upper edge helped cracks initiate from uneven heating, and a denser grade of graphite was used (GR030 to GR001cc). It was preheated in a separate furnace at around 150°C for several hours before starting the 300°C/hour high-temperature ramp. Sadly, the new crucible also failed.

Experiment 3

For the third experiment, extensive changes were made in order to solve several issues present in 1 and 2. Firstly, to prevent any further crucible issues, a secondary containment crucible was added and both crucibles were heated in the furnace overnight at 150°C before the ramp to high temperature, which would be limited to 200°C/hr. Secondly, the Inconel drive shaft experienced warping from temperature cycling, leading to issues with vibration shaft alignment, as well as being difficult to move vertically through the lid bearings. The rotary system was therefore

switched to a modified rotary degasser which was already present in the laboratory, shown in Figure 11. The degasser used a 1.5in. OD graphite drive shaft with the capability of providing gas flow through the shaft. Graphite baffles were integrated into a modified furnace lid and were able to move vertically and lock in position. Full-length baffles were not used, due to the risk of impeller blades impacting the baffles if either were slightly misaligned.

In order to adapt the degasser to the ISGR process, the existing drive shaft on the degasser was replaced with one that was internally threaded at one end. A model of the assembly is shown in Figure 12. Threaded into the drive shaft is a graphite linkage shaft, which at the other end is cemented to the inner walls of the impeller. In the event of impeller or linkage shaft failure, the drive shaft could therefore be re-used.

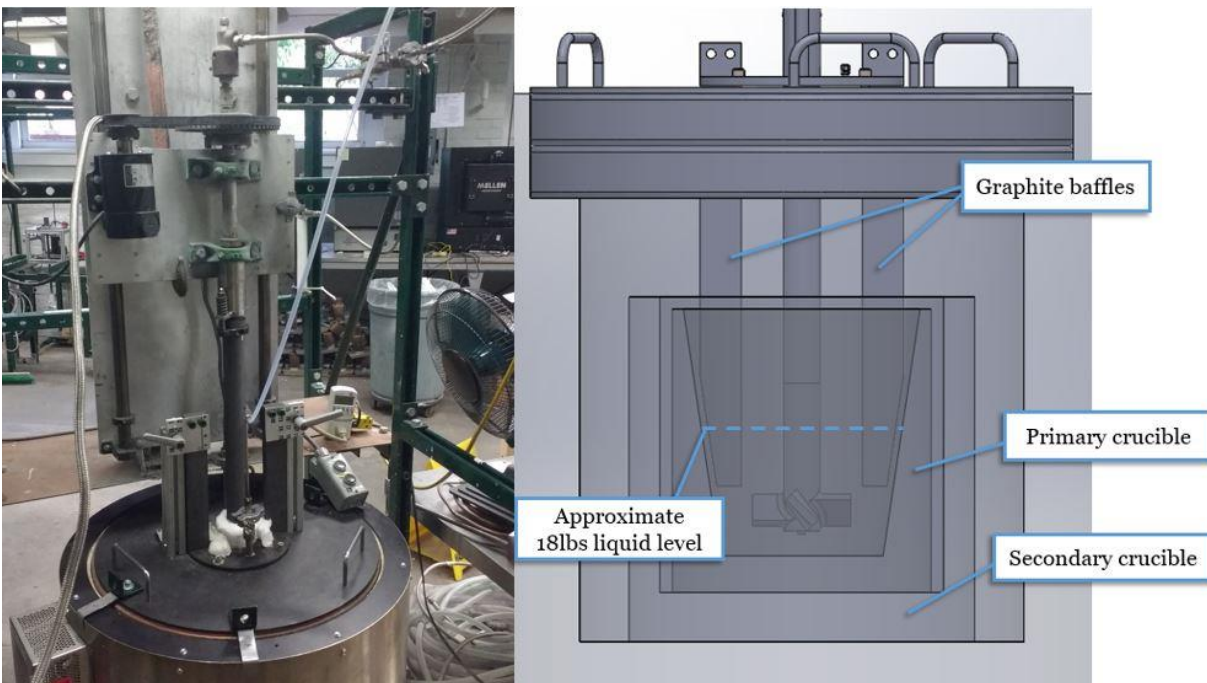


Figure 11: Rotary degasser-based ISGR apparatus used in experiments 3 and 4

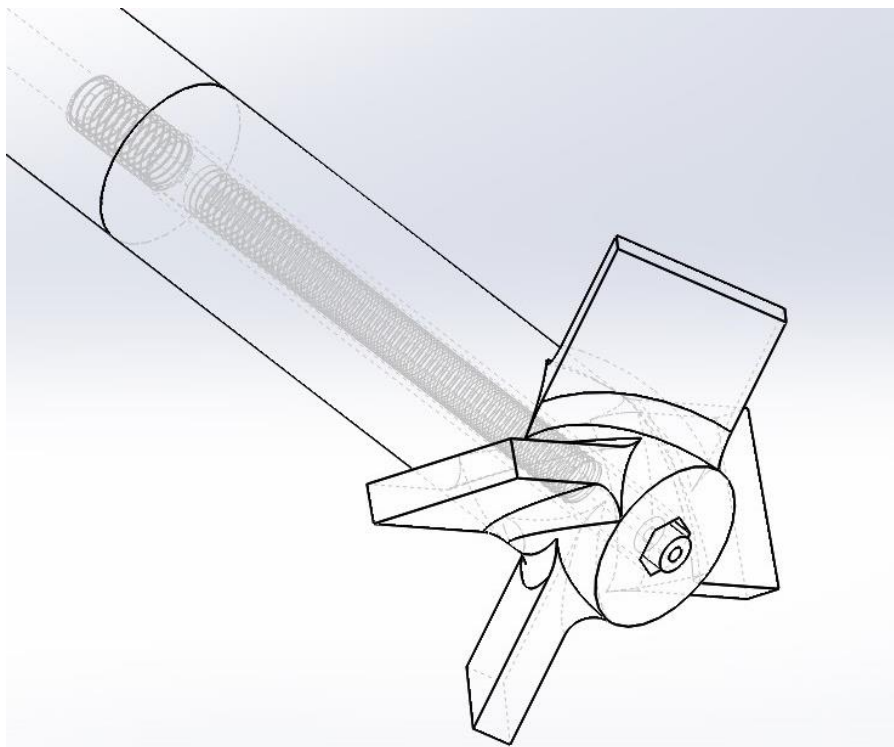


Figure 12: Impeller assembly showing the threaded graphite linkage to the rotary degasser shaft, and an example of a possible gas nozzle

Nitrogen was allowed to flow for 150 minutes at a rate of 4L/minute while being stirred at 250RPM, and the temperature was maintained between 1025-1050°C. Except for a small amount of metal splashing out of the crucible into the space within the secondary containment, the experiment appeared to be successful.

Experiment 4

For this experiment, the temperature during the reaction was maintained between 1039-1040°C for 100 minutes. The nozzle at the end of the impeller was also switched to the protruding tip. Ideally, experiment 4 would have had only the reaction time decreased while maintaining the same nozzle, followed by at least one more experiment to compare nozzle types. In the interest of time, L4 was set to the configuration which was anticipated to result in the best material. The experiment appeared to be successful, and the ingot shape indicated the molten material was less viscous.

Since the motor torque was expected to correlate to increases in viscosity caused by particle formation, motor current was measured for experiment 4 in order to correlate the material results with current in order to provide a guideline for the reaction time of future experiments. Calculating mixing power from input current is less accurate than measuring directly using a device such as a torque transducer, but in the interest of time the current measurement was used as a rough estimate.

To obtain an estimate of the portion of the current actually applied to mixing, ammeter measurements were taken from the AC line leading to the motor controller once in a no-load condition where the impeller rotated freely at 250RPM, then continuously during the reaction.

Power was calculated using equation 13.

$$P = \eta V(I - I_0) \quad (13)$$

Where η is the efficiency of the motor (unknown but estimated at 0.75), V is the voltage, (112.7V), I is the measured current while stirring the melt and I_0 is the no-load current.

2.2.3 Glycerin/water fluid model

Soon after the large-scale ISGR experiments began, it became clear that the large amount of time required to set up and run ISGR experiments justified using a cold fluid model in order to speed up optimization of the process, especially since the gas dispersion ability of the two gas insertion configurations was not well-understood. The following images were taken from 120fps videos of several mixing configurations as well as bubble formation in an unmixed tank.

An important note on the mixing model: this was intended to approximate the viscosity of molten Al at 1050°C. However, the glycerin/water ratio was set at 65wt% glycerin for 15cP³⁵ based on a decimal place error, as the real viscosity is closer to 1.5cP.³⁶ This may be a negligible difference, since the same mixing techniques are normally used for liquids below 5000cP which is considered “low viscosity.”³⁰ Regardless, other variables such as the addition of particles and differences in surface tension make the hot system challenging to model accurately. The value this model is that it can be used to compare the mixing characteristics of different arrangements relative to each other, but not much can be found quantitatively.

The four mixing configurations tested were an unbaffled system with the gas through either the end of the impeller, or a separate tube, and the same in a system with two baffles constructed to be close to the dimensions of those in the hot process. The mixing setup is shown in Figure 13. A flat-sided glass jar was used instead of imitating the slanted crucible, since the optical distortion would not be as problematic. Different nozzle types, as introduced in section 2.2.2, were compared with and without stirring.



Figure 13: mixing setup showing position baffles and gas insertion tube in glycerin/water mixing tank. Impeller height was set to 1in. from the tank bottom, and tube height 0.75" from the upper edge of the impeller blades.

2.3 SHS approach

2.3.1 General process

This process evolved over time and was attempted in both a two-step melting procedure where master alloy was first produced at WPI as shown in Figure 14, as well as a single-melt process. Variations on this process will be explained for individual experiments, and the various reactant powders used are listed in Table 1.

Pellet production:



Al, Ti, C ball milled



CuO added, then paint shaker mixing to avoid fire hazard



30mm OD pellets pressed at 200 MPa
OR loosely-wrapped foil packages

Reaction:



Pellets held under melt
~760°C minimum temp.



Thermite reaction
activates TiC reaction



Cast samples, analyze,
possibly re-melt for ultrasonic
processing and squeeze
casting/gravity casting

Figure 14: general sequence of powder preparation and master alloy production. Pellets were preheated for at least 2 hours at 100°C immediately before the reaction.

Table 1: Powders used in SHS experiments

Composition	Supplier	Particle size	Purity
Carbon (graphite)	SkySpring Nanomaterials	<100nm	Unspecified
	Alfa Aesar	7-11µm average	99%
Titanium	Stanford Advanced materials	600nm average	99%
	Atlantic Equipment Engineers	<20µm	99.7%
	Atlantic Equipment Engineers	-325 mesh (<44µm)	99.7%
Copper (II) oxide	Millipore Sigma	<10µm	98%
Aluminum	Alpha Chemicals	30µm average	99.5%

The original plan was to send out material once there was enough made to produce several squeeze-cast plates from a diluted material. This procedure was later modified after it was found to be challenging to properly mix re-melted composite into the dilution alloy at the maximum temperature of the Eck furnace, ~775°C. After this, experiments were run as either small batches

at WPI which were only analyzed after reaction without ultrasonic, or a procedure where pellets were reacted directly in a larger furnace at the Eck squeeze-casting facility, with simultaneous ultrasonic processing.

2.3.2 Experiments

Selected experiments are introduced here, numbered in chronological order. A variety of batch sizes, melt temperatures, powder compositions and other variables were explored.

Experiment 1: nano/submicron reactants

Initially, nano/submicron-sized titanium and graphite reactant powders were used along with micron-size Al. Using Ti and C powders of this size would not make for an economical process, though it was expected that this would produce very fine reinforcements, and therefore it could be judged if future micron-size reactants were too large to produce similar particles. The powders were combined at a ratio of 1 mol each Ti and C, 1.5 mol Al, mixed on a slow-speed jar mill for 24hrs and pressed into pellets of ~16g each. Pellets were fragile, possibly because of the carbon powder, but could be held together if wrapped in a sheet of Al foil as a carriage to be held with tongs. This is shown in Figure 15 along with the tool used to submerge the pellet under the melt surface to minimize oxidation. These pellets were reacted in pure Al.

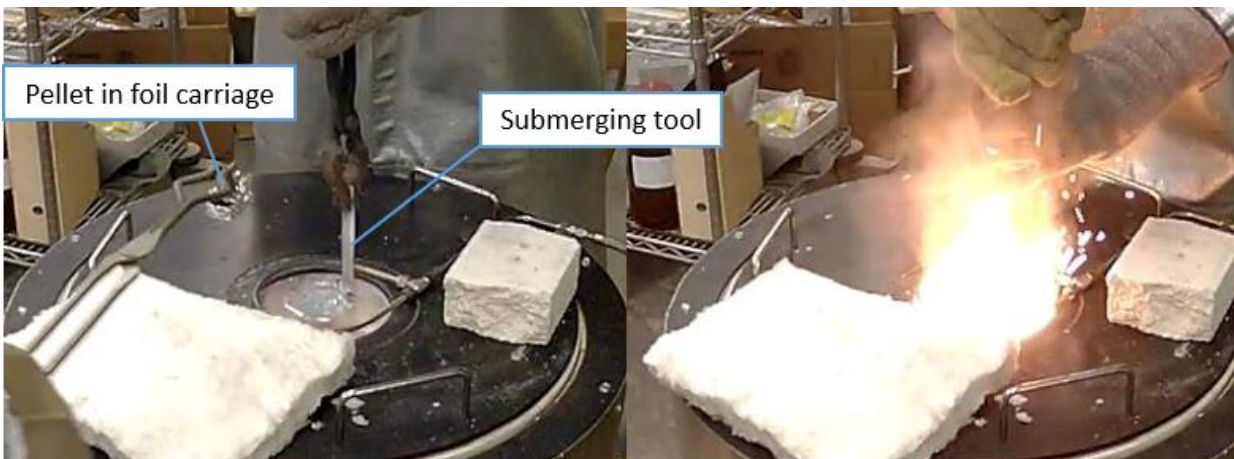


Figure 15: reaction during experiment 1

A perforated tube with argon flowing above the crucible was used, with the intention of minimizing the effects of oxygen entrained in the melt from the foil. However, the oxygen level detected near the surface of the melt was not significantly lowered and this was considered not to be worthwhile.

Experiment 2: Initial use of micron-size reactants

The next experiment used entirely micron-size reactant powders, in the same ratio as before as well as the addition of 0.1 mol CuO, using 7-11 μ m carbon powder and -325 mesh Ti powder. These pellets were durable enough to grip by hand, or gently using tongs. The mixing method was a Resodyn Resonant Acoustic Mixer with the help of Dr. Zhenzhen Yu of CSM. The RAM is a non-impact mixing device, used because there was evidence from previous work that ball milling a powder mix which included CuO would be a fire hazard, even on a slow jar mill. The reaction was done in pure Al, and in an induction furnace. Using the induction furnace allowed for improved control over the melt temperature, which increased significantly when pellets were reacted in small amounts of Al. The well-insulated resistance furnace used in experiment 1 was inconvenient due to the waiting time to cool the melt between reactions and the slower heating rate. Dilution in A356 along with UD was performed at WPI for this experiment, and these were gravity cast into tensile bars.

Experiments 3-8: Variation of mixing method and composition

A series of similar experiments were carried out in order to determine the effect of changing levels of C and CuO, as well as whether the RAM processing was necessary. The alternate mixing process was to mix Al, C and Ti on a ball mill, remove the milling media, add in CuO, then shake the powder by hand for 2 minutes. Reactions were done in ~500g of pure Al, with the powder proportions and mixing techniques shown in Table 1.

Table 2: mixing method and powder levels for experiments 3-8

Experiment	Mixing method	CuO level	Carbon level
3	Ball mill + hand shake	Baseline	Baseline
4	RAM	Baseline	Baseline
5	RAM	Baseline	+10%
6	RAM	+55%	Baseline
7	RAM	+55%	+10%
8	Ball mill + hand shake	+55%	Baseline

Experiment 9: Initial use of intermediate size Ti powder

From this point onward, the paint mixer from Figure 14 was used instead of shaking the CuO by hand into the remainder of powder, to ensure consistency. The pellet density was increased, which improved pellet strength. Starting with this experiment, the intermediate-sized <20 μ m Ti powder was used.

Experiments 10 & 11: Loose powder reactions using large packets

Several experiments were done using loose powder wrapped in foil packets instead of pressed pellets. The first two, experiments 10 & 11, used micron-scale powders for all but the carbon, with nanoscale carbon used. This powder was mixed using the same methods as previous experiments. Squares of Al foil were cut, formed into bowl shapes, filled with powder and closed, forming packets which were approximately the size of the densely-pressed pellets. When these ignited, a significant amount of unreacted powder floated to the top and oxidized.

Experiments 12 & 13: small versus large batches

These experiments to compare the reaction of dense pellets at WPI versus Eck, both in alloys close to Al-7%Mg and with the Eck material squeeze-cast after ultrasonic processing.

Experiments 14 and 15: smaller foil packets

Packets with a diameter close to 15mm as well as micron-size carbon were reacted in Al-7%Mg as well as A356. The smaller packet size was used in order to prevent powder from scattering out of the reaction zone and floating to the surface.

Experiment 16: broken pellets

Dense pellets which were broken into pieces, in order to shorten preheating time as well as determine whether the size of the pellet had a significant effect on the resulting material. Breakage was not precise, but pieces were generally 4g or less.

Experiment 17: ignition from one end

A modified pellet formulation was used in order to test how well the reaction could self-propagate in the melt when the thermite reaction only occurred at one end. The bottom 1/5 of the pellets contained the same ratios of powders as recent experiments, and the top 4/5 contained no CuO.

Experiment 18: comparison of multiple matrix alloys

The final set of experiments, 18a, b and c, compared plates cast from alloy P1020 (>99.7%Al) reinforced with TiC produced from dense pellets, as well as the same with 7wt%Mg added in and finally a plate containing the Al-xTiC-7%Mg with approximately 1wt% Ni. The properties were then compared to a reference plate of plain P1020.

To summarize, these experiments are listed in Table 3 along with the alloy pellets were reacted in as well as the pellet type. Early experiments were performed using enough powder to produce ~10vol% TiC, under the assumption that they could be diluted later. For small batches, each pellet reaction increased the temperature of the melt significantly which made temperature control inconvenient. Starting with experiment 10, all were performed in a powder/melt ratio to produce ~2vol% TiC. This resulted in larger melt volumes for the small batches, minimizing the temperature swing.

Table 3: SHS experiment summary

Experiment	Matrix	Pellet type
1	99.99% Al	Pressed
2	99.99% Al & A356 dilution	Pressed
3	99.99% Al	Pressed
4	99.99% Al	Pressed
5	99.99% Al	Pressed
6	99.99% Al	Pressed
7	99.99% Al	Pressed
8	99.99% Al	Pressed
9	99.99% Al	Pressed
10	Al-7% Mg	Large foil packets
11	99.99% Al	Large foil packets
12	Al-7% Mg	Pressed
13	535	Pressed
14	A356	Small foil packets
15	99.99% Al	Small foil packets
16	99.99% Al	Pressed & broken
17	99.99% Al	Pressed, CuO only at one end
18a	P1020	Pressed
18b	P1020 + ~7%Mg	Pressed
18c	P1020 + ~7%Mg + ~1%Ni	Pressed

3 Results and Discussion

3.1 ISGR

3.1.1 Small-scale system

The material produced in experiments 3 and 4 was characterized using scanning electron microscopy with energy-dispersive x-ray spectroscopy (SEM-EDS) along with X-ray diffraction (XRD). To have a better chance of seeing small AlN particles, polished ISGR samples were etched for 10s in 10wt% NaOH solution followed by a 30s water rinse. The experiment 3 and 4 master alloys contained AlN, but most particles were longer than 1 μ m. Though it was not expected to perform well in tensile tests, ultrasonic processing was applied in order to test the device, and tensile specimens of the material diluted in A356 (approx. 1:4 ratio of composite to A356) were gravity-cast in steel molds. There was not a significant increase in strength, and the fracture surfaces contained clusters of AlN platelets.

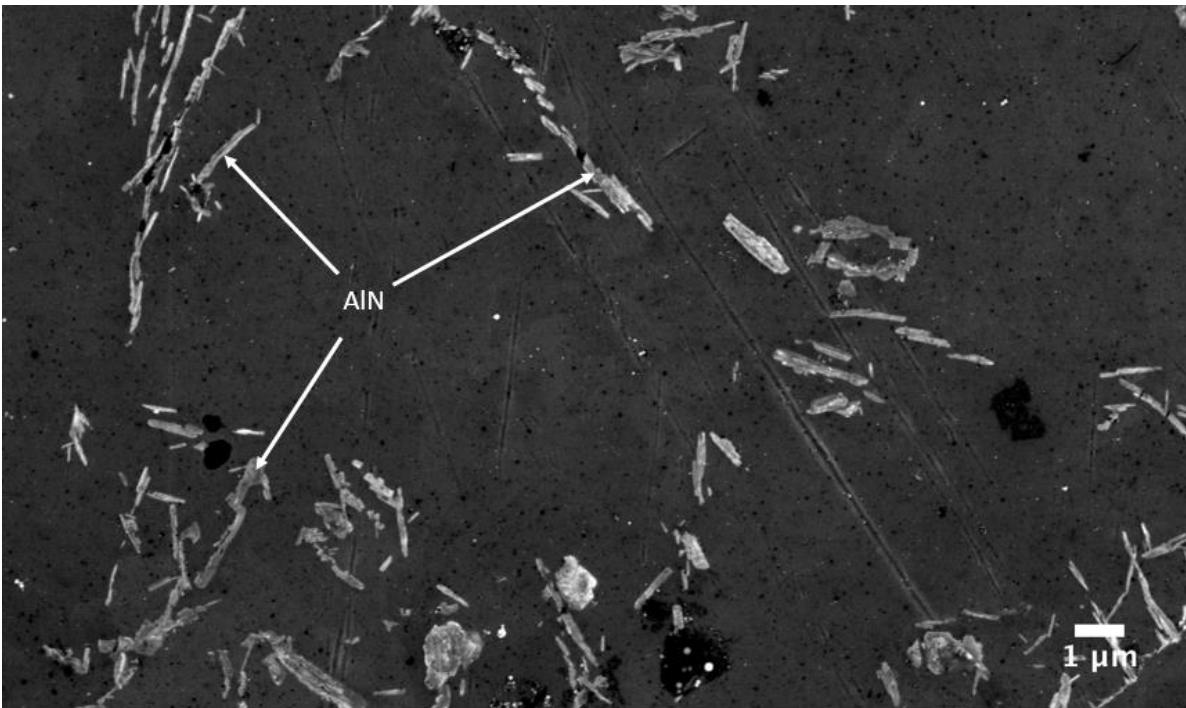


Figure 16: SEM micrograph of ISGR small-scale master alloy. This and most other SEM, XRD and EDS images were provided by collaborators at the University of Michigan.³⁷

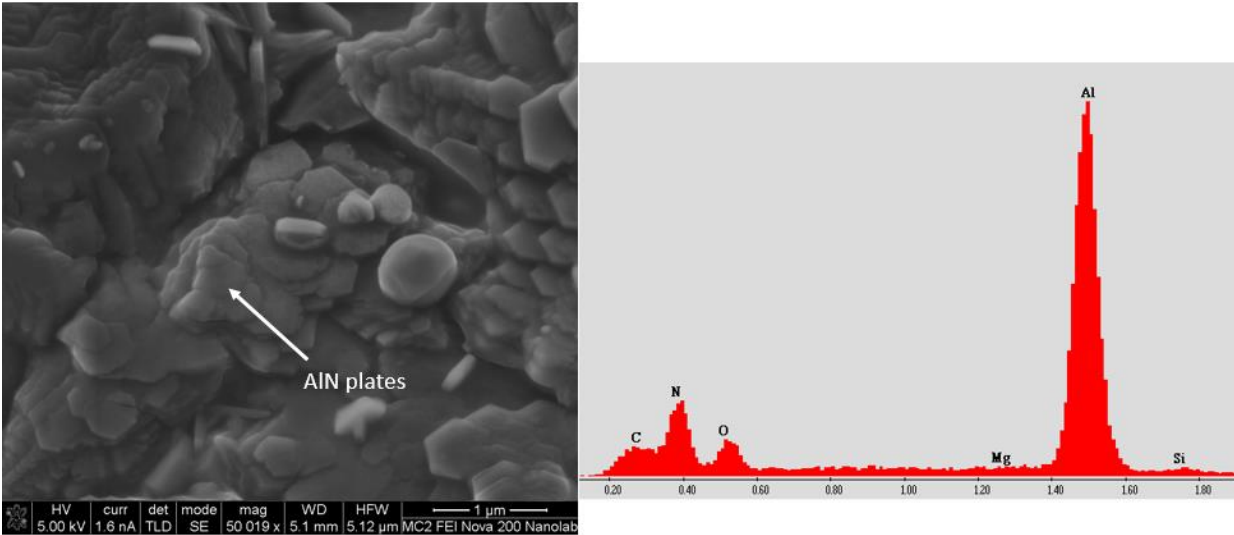


Figure 17: SEM micrograph with corresponding and EDS point on diluted ISGR fracture surface.

The growth of micron-scale particles could be accounted for by the mixing characteristics of the impeller, which likely subjected the gas bubbles and surrounding metal to less shear force than was required to keep particles in the nano range. It was concluded that for the next experiments, four-bladed impellers should be used.

3.1.2 Large-scale system

A sample from experiment 1 was analyzed just in case AlN had formed before the crucible leakage, but none was found. Experiment 2 material was not useful because the crucible failed before the reaction. There was a benefit from these experiments: besides motivating changes in the crucible design and preheating procedure, one of the failed experiments also proved the strength of the new impeller. During experiment 2, the shattered crucible entered the path of the spinning impeller, stalling the mixing motor but leaving the impeller unharmed.

Experiments 3 and 4 were partially successful. A cross-section of the material from experiment 4 after removal from the crucible is shown in Figure 18.

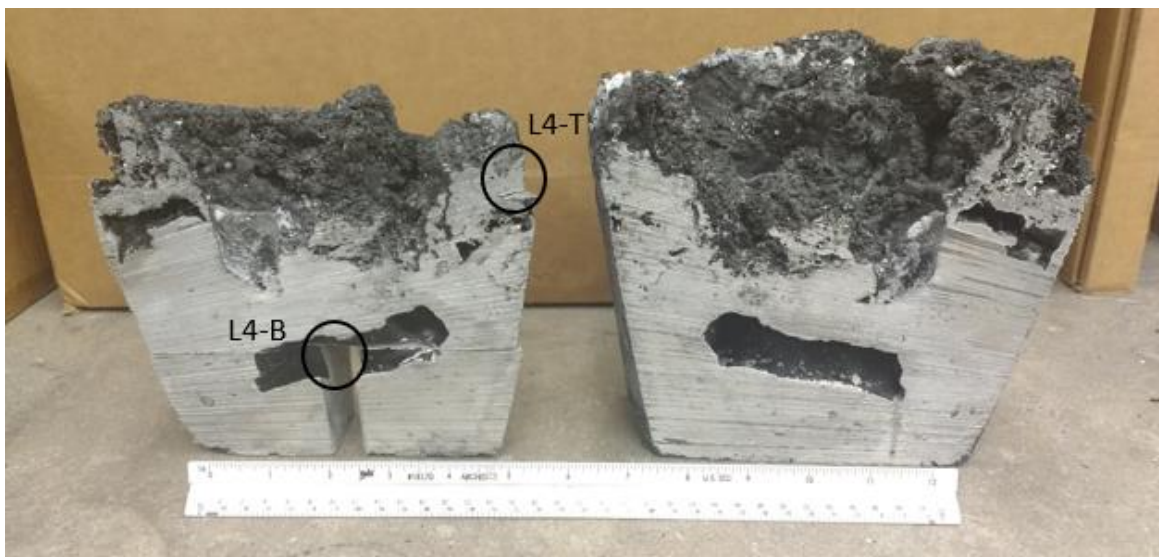


Figure 18: large experiment 4 composite material cross-section with sample locations marked. L3-B and L3-T samples were cut from similar locations

SEM and EDS results are shown for L3 before dilution in figures Figure 19 and Figure 20. EDS was used to identify AlN and possibly aluminum oxynitride in L3-B. L3-T contained nanoparticles which were assumed to be AlN, though they were too small to be identified using EDS and the sample was too rough for good XRD results. The large AlN particles seen in L3-B were similar to those seen in small ISGR experiments and were the primary motivation for decreasing the reaction time when moving on to experiment L4. The time change was arbitrary, but with the consideration that it should still run long enough that the ammeter reading had increased noticeably in case this was evidence of nanoparticle formation.

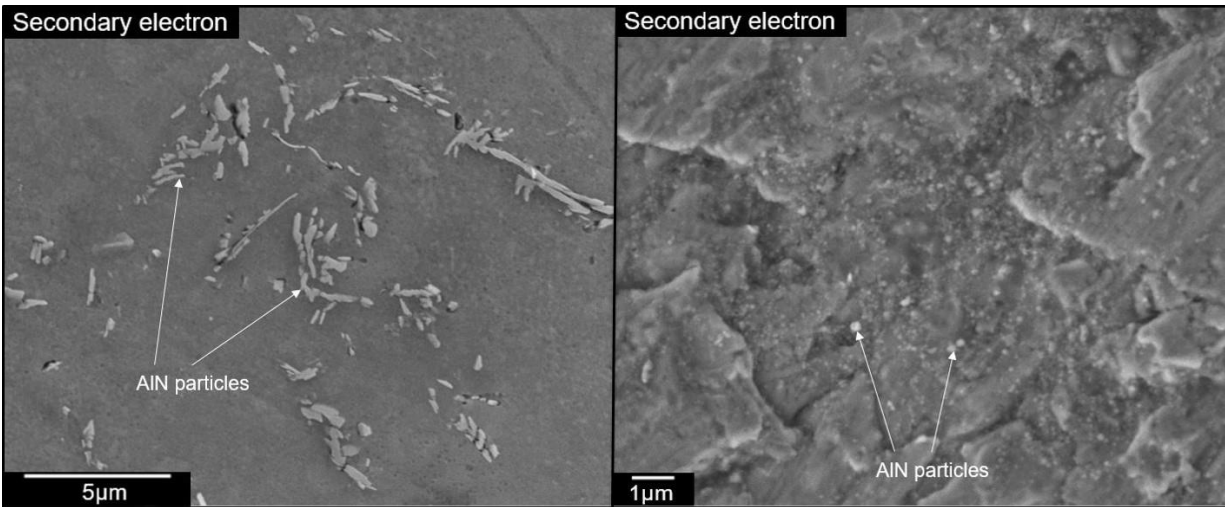


Figure 19: L3-B sample on left, and L3-T on right. Particles on right most likely AlN, though not definitive.

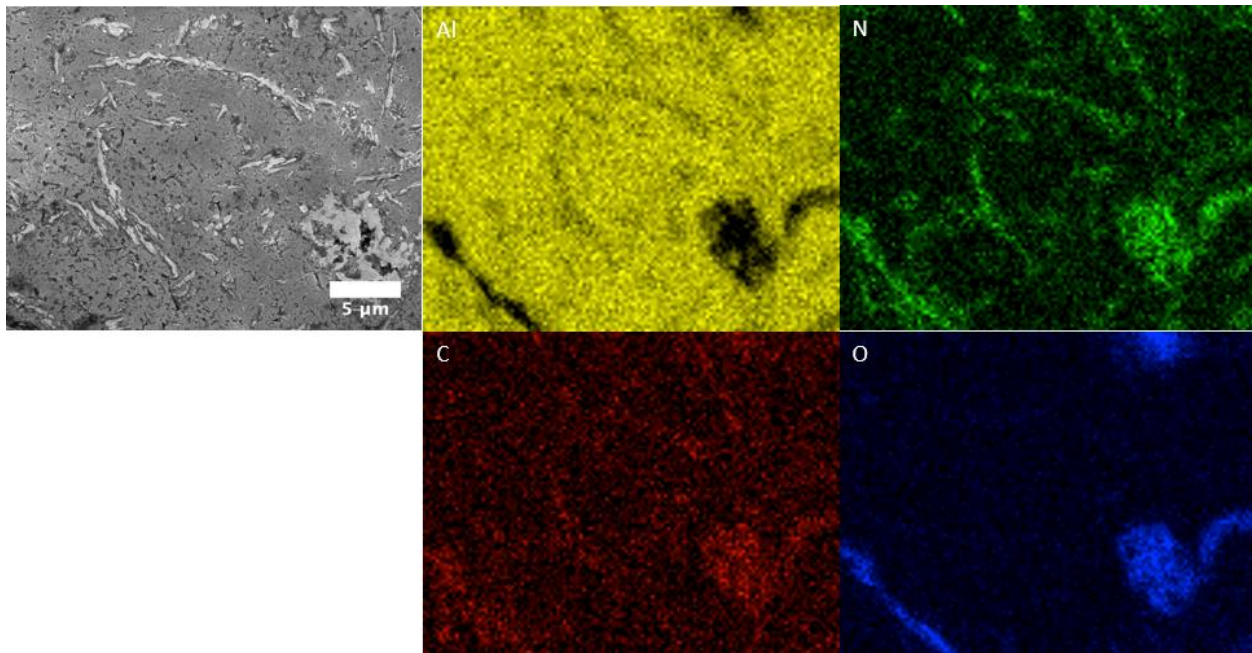


Figure 20: EDS maps for another area of L3-B, with possible mixed oxides and nitrides or oxynitrides in some areas.

In Figure 21, AlN is seen in the XRD spectrum in sample L4-B. Nanoparticles were not seen in L4-T, though the high-resolution SEM usually used was not available in time to have conclusive results on that sample. As with L3, the top sample was too rough for XRD. Similar elongated particles were seen in SEM analysis.

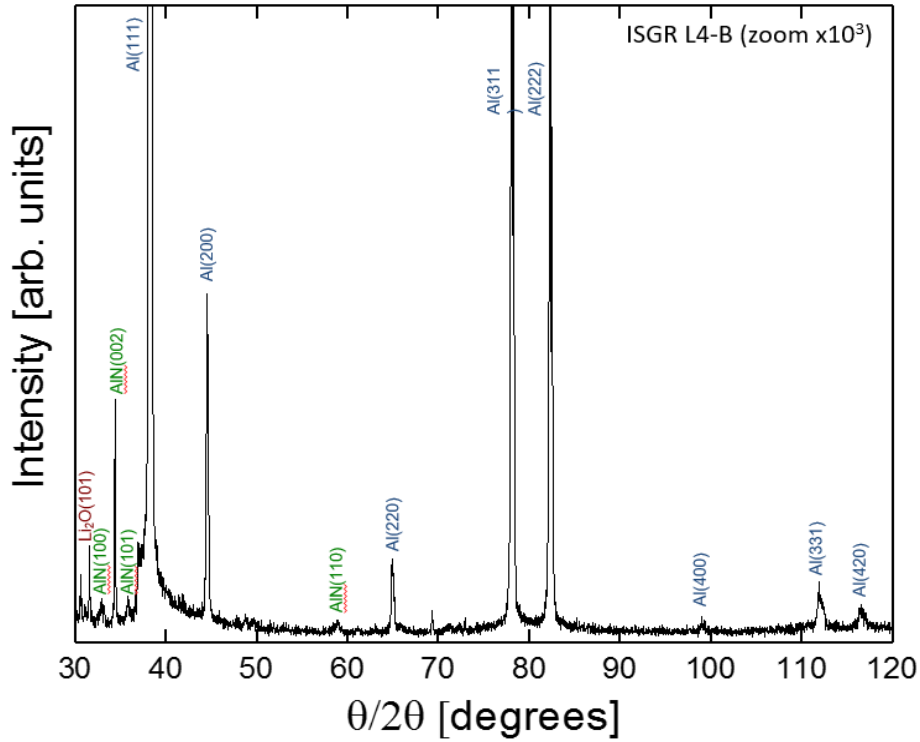


Figure 21: XRD spectrum for sample L4-B.

The mixing shaft power calculated from amp measurements during experiment L4 is plotted in Figure 22. Measurements were recorded from a video of the multimeter display, and each data point was a time-averaged over 3 seconds to account for variability from the shaft rotation and fluid mixing instability.

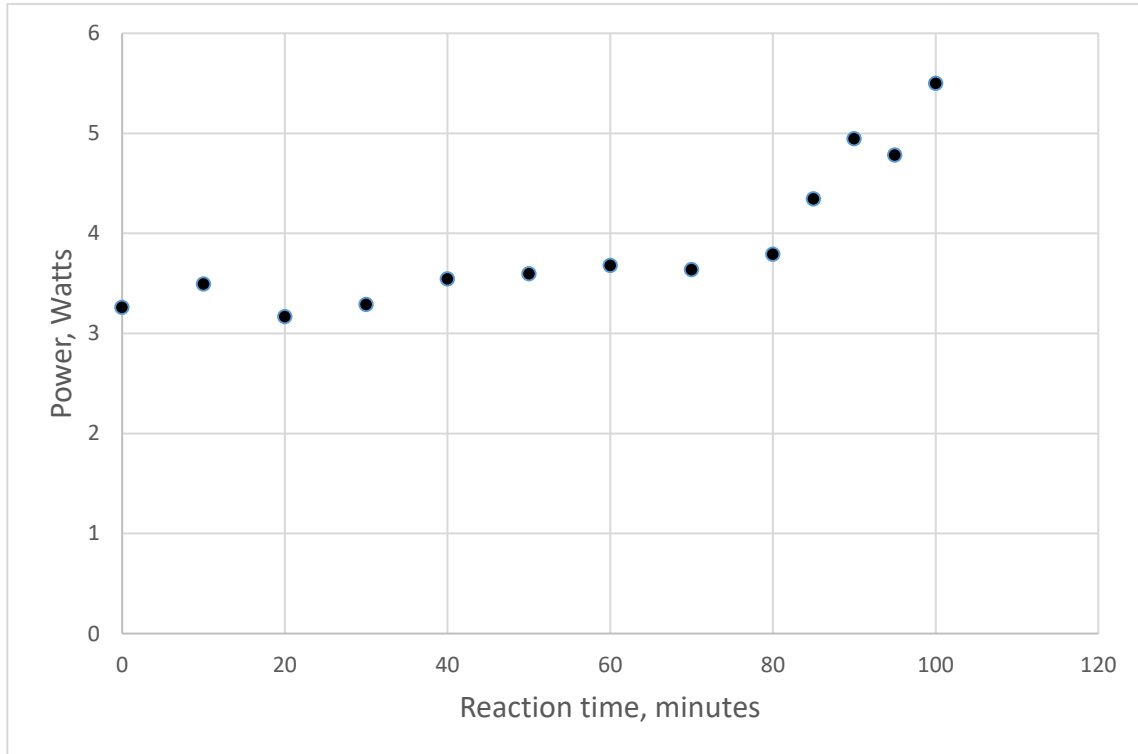


Figure 22: Plot of mixing shaft power vs. time for experiment L4

Material from the top half of experiment 3 was diluted in A356 along with ultrasonic processing at Eck, since there was evidence of nanoparticles in the top but not the bottom. Mixing of the composite material into the dilution melt was challenging, likely because of the extraneous phases which developed on the top surface of the ISGR ingot during master alloy production. The squeeze-cast material did not appear homogeneous, and hardness measurements did not show any increase.

3.1.3 Glycerin/water fluid model

Unbaffled mixing, in Figure 23, behaved as expected, though the central vortex extended surprisingly far down the impeller shaft. Most of the bubbles exiting the nozzle showed limited dispersion in the region level with the impeller blades but were instead dispersed by interacting with the vortex. Without gas flow, there was also some amount of air entrained in the liquid over time.



Figure 23: unbaffled mixing test, 200 and 250RPM

For baffled experiments, 150, 200, 250 and 300 RPM were tested. At 150, the impeller was entirely flooded, with bubbles remaining roughly at their starting sizes and rising immediately to the surface. Starting at 200, small bubbles were seen recirculating. At 250, bubbles were rarely visible rising to the surface without being sheared, and at 300, none were visible. After enough time at 200-300RPM, gas would be dispersed well enough that when the flow stopped, the liquid appeared cloudy and took ~10 minutes to return to normal. When the same mixing conditions were filmed using the protruding nozzle as well as the separate gas tube, gas dispersion appeared to be very similar.

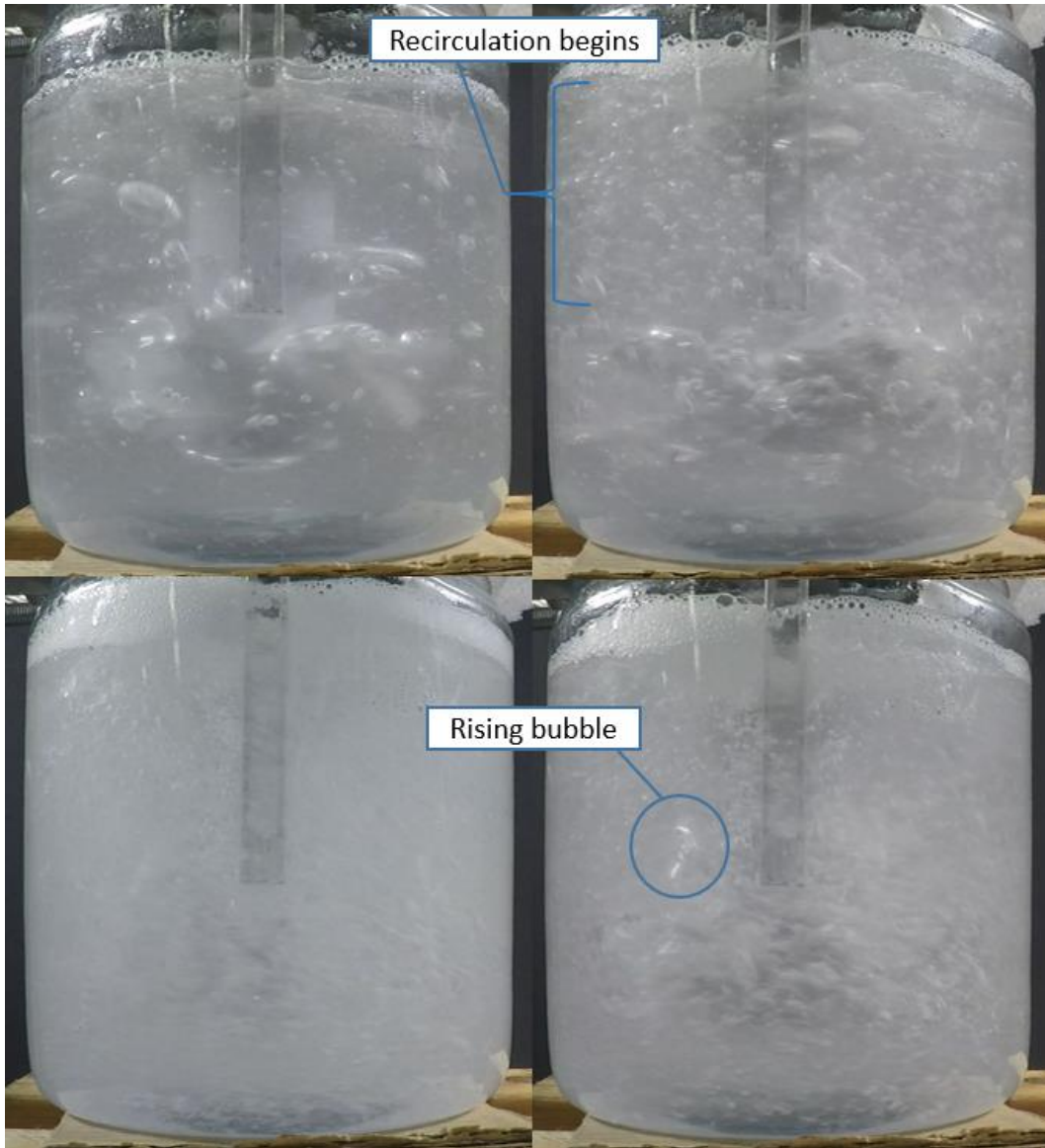


Figure 24: Baffled tank, clockwise from top left: 150, 200, 250 and 300RPM

In Figures 25, 26, and 27, bubbles were recorded in an unstirred tank from three different nozzle types. Bubble diameter was difficult to measure reliably, as it varied from frame to frame, though the rate of bubble rise was lowest for the six-hole nozzle and highest for the flat single hole. In the case of the six-hole nozzle, gas emerged mostly as two separate bubbles, and sometimes three. Flow rate was increased up to 7000mL/min., which had the effects of increasing bubble frequency and a slightly increased maximum bubble depth, but there was no noticeable change in bubble size.

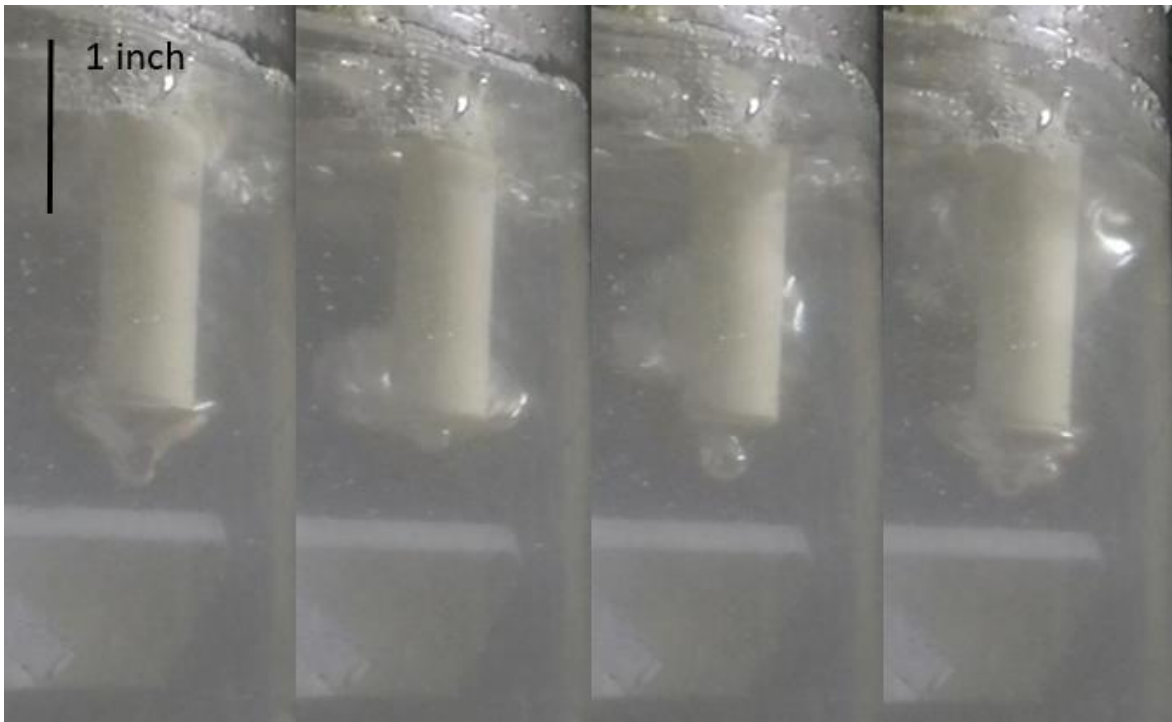


Figure 25: flat single-hole nozzle, 4000mL/min.

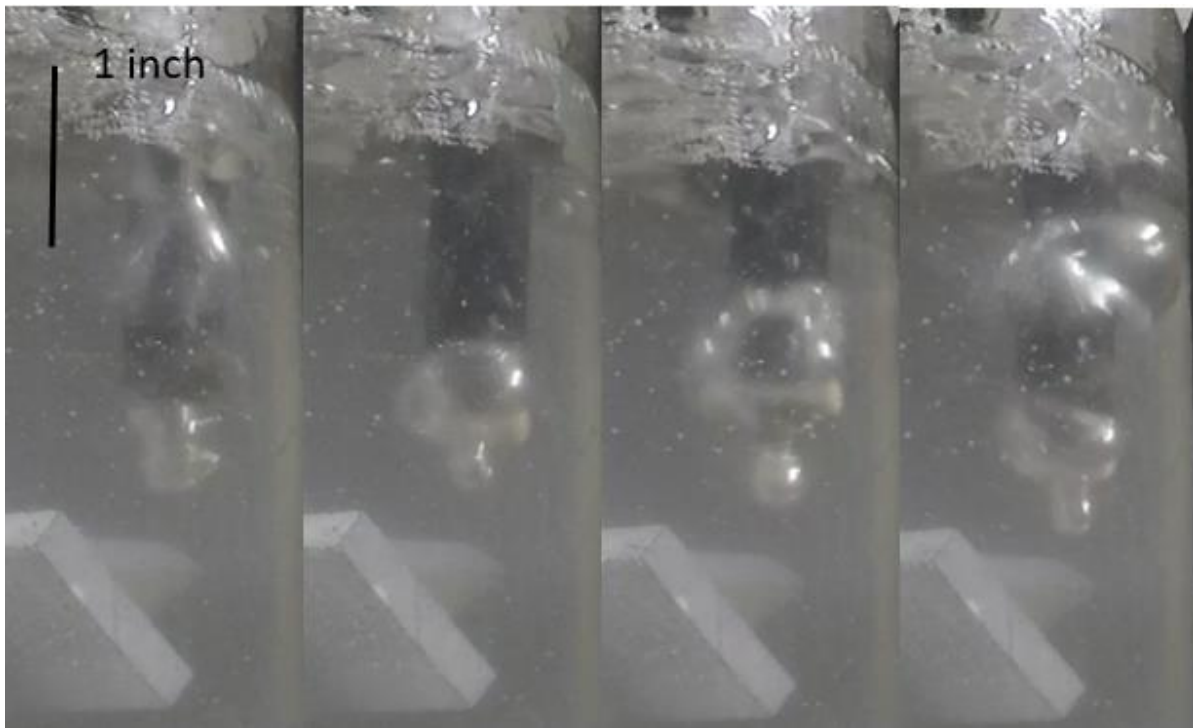


Figure 26: protruding single-hole nozzle, 4000mL/min.



Figure 27: six-hole nozzle, 4000mL/min.

In Figure 28, bubbles were recorded in an unstirred tank entering from the bottom of the impeller. A flat single-hole nozzle was also tested, with the same result except for the lack of a pointed end to the bubble.

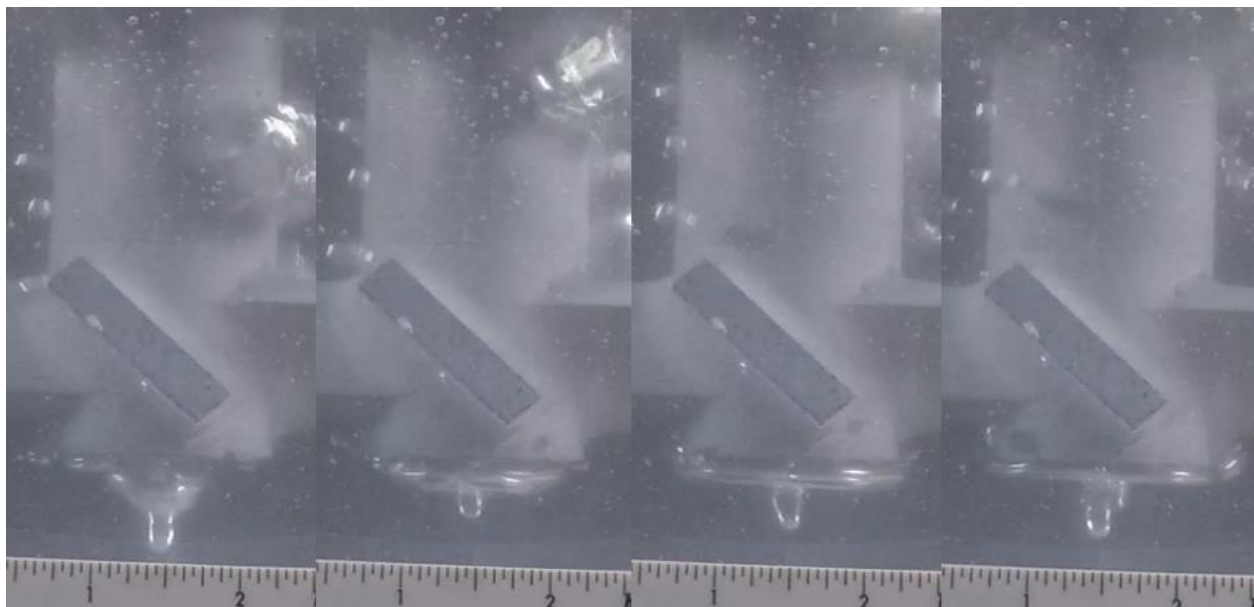


Figure 28: protruding single-hole nozzle, 4000mL/min.

3.1.4 Discussion

The ISGR experimentation proved to be extremely challenging, and particle size control remains a stubborn issue. The nanoparticles seen in the upper region of L3 and L4 are assumed to be AlN, but ideally transmission electron microscopy should be done on those samples to be sure, and to observe the interface with the matrix.

The connection between mixing parameters, fluid viscosity and particle formation

Observing the glycerin/water model, gas insertion from the end of the impeller and from a separate tube above the blades appear to perform similarly in terms of gas dispersion. Though the separate tube adds complexity to the system, it allows gas to enter the system at a location which is closer to that of the successful small-scale experiments. It is possible that the Al-AlN process performed well despite the unbaffled arrangement because the gas holes were at the impeller tips where they would experience a high shear rate immediately after entering the liquid. Further work with a separate gas insertion tube would be necessary in order to determine if that arrangement removes problems of large particle growth seen after the impeller tip gas flow. As for the design of the gas nozzle, a multiple-hole design as well as the single protruding nozzle could both be good options to explore. Traditional sparger systems which consist of rings or tubes placed above or below the impeller could also be possible, though designing them to withstand the hostile conditions would be quite a challenge.

More rigorous fluid models which can approximate the hot process more closely could provide valuable information for optimizing the process and could include close observation of bubbles emerging from downward-facing nozzles while being stirred. Measurement of gas bubbles in molten Al is also possible, as in the study by Gnyloskurenko and Nakamura wherein argon bubble detachment from nozzles in Al was observed by x-ray.³⁸ If a similar setup could be constructed for similar observations of nitrogen bubbles in Al, especially with the ability to measure the force necessary to break up a bubble, this could be also be valuable.

All the ISGR experiments that produced AlN had large amounts of metal stuck to the impeller, as well as solidified ingot shapes indicating that the material became highly viscous. This may be largely from effects of the micron-scale plates as opposed to the nanoparticles. Plates and acicular

shapes have been shown to increase apparent viscosity to a larger degree than spherical particles at the same vol%,³⁹ so reaction time may need to be shortened to end before the sharp increase in mixing power which was observed at ~80 minutes for L4. The rheology of nanofluids, especially metal ones, is not well understood, but there has been work on measuring the viscosity of AlN-propylene glycol suspensions. Yu et al. reported that a suspension with 5vol% AlN increased the viscosity by 75% versus the , but above 5% the fluids showed shear-thinning behavior.⁴⁰ For ISGR, this means that the high shear rate of the impeller could limit the increase in viscosity as particles form.

If the nanoparticles do not have a large effect on the viscosity of Al in the volume fraction and shear rate ranges and of the ISGR process, measurements from a sensitive torque transducer could be useful in quantifying the torque versus volume fraction. Optimization will then require improving mixing and gas dispersion as well as determining the correct time to end the reaction. Viscosity of the molten composite could be measured, but that could be a difficult experiment that may not be worth the trouble.

Hardware considerations

The number of hardware inconveniences and breakages limited the number of experiments which could be run. There were several bright spots in the hardware scale-up though. The new impeller design turned out to be a significant improvement in the system as it was extremely durable and showed no obvious signs of corrosion, which the previous 3D-printed impellers were susceptible to. The switch to a graphite drive shaft was also an improvement, in terms of reducing oscillation and misalignment of the impeller and allowing for trouble-free vertical motion. (add some more)

An issue that needs to be solved before this process could be applied for industrial use is the furnace and crucible arrangement. All large ISGR ingots were challenging to remove from the crucible, despite the use of a sacrificial crucible coating. Generally, they could be removed with the use of ethanol sprayed into the interface, a Dremel tool to grind away obstructions, and a hammer and chisel to encourage the ingot to break loose. A crucible with a removable plug to allow the material to exit while molten could be considered, though it could be challenging depending on the fluidity of the liquid and would require the mold to have a protected atmosphere due to the lithium content.

3.2 SHS

3.2.1 Results

Experiment 1: Nano/submicron reactants

Melt temperature was measured at an average of 862.5°C. APS could not be measured accurately for experiment 1 due to clustering of particles and issues with polishing, but most were between 100-400nm. Many oxides and intermetallics were observed through use of EDS.

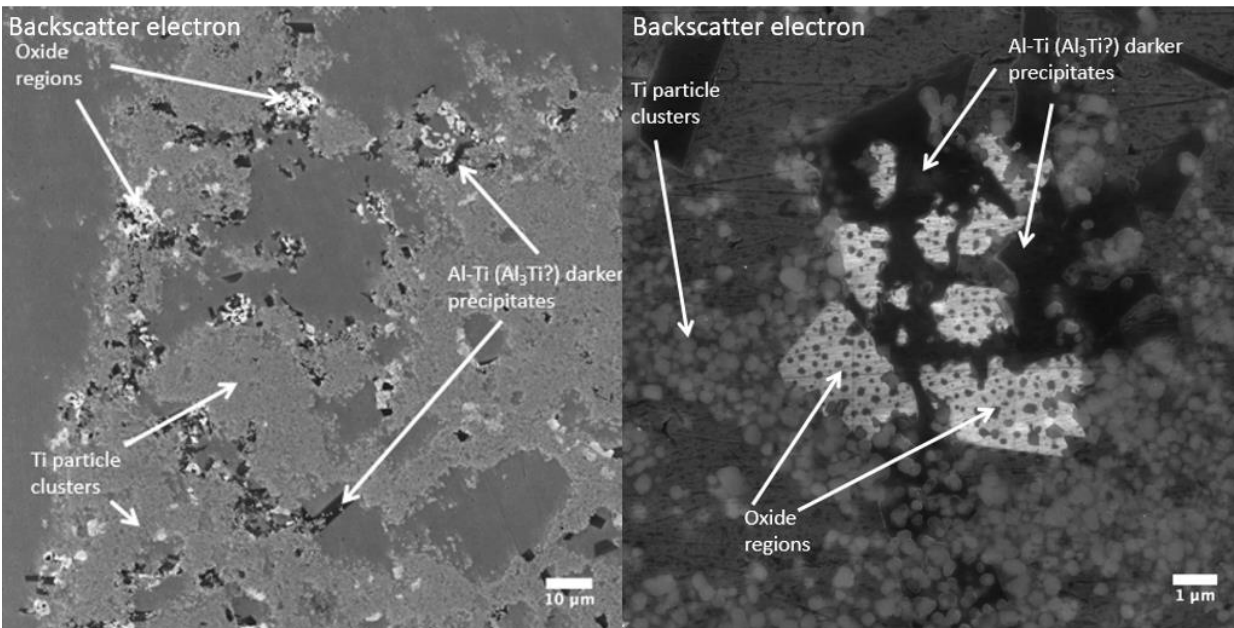


Figure 29: experiment 1

Experiment 2: Initial use of micron-size reactants

This was the first use of the induction furnace for SHS, so temperature control was not precise, being measured at an average of 881 ± 34°C. Particles were larger than in the previous batch, with an APS of 1250 μm.

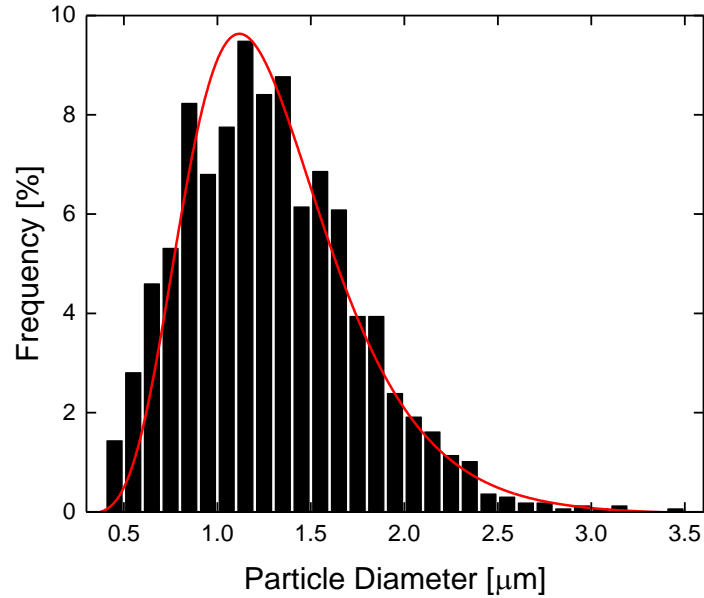


Figure 30: experiment 2 TiC particle size distribution.

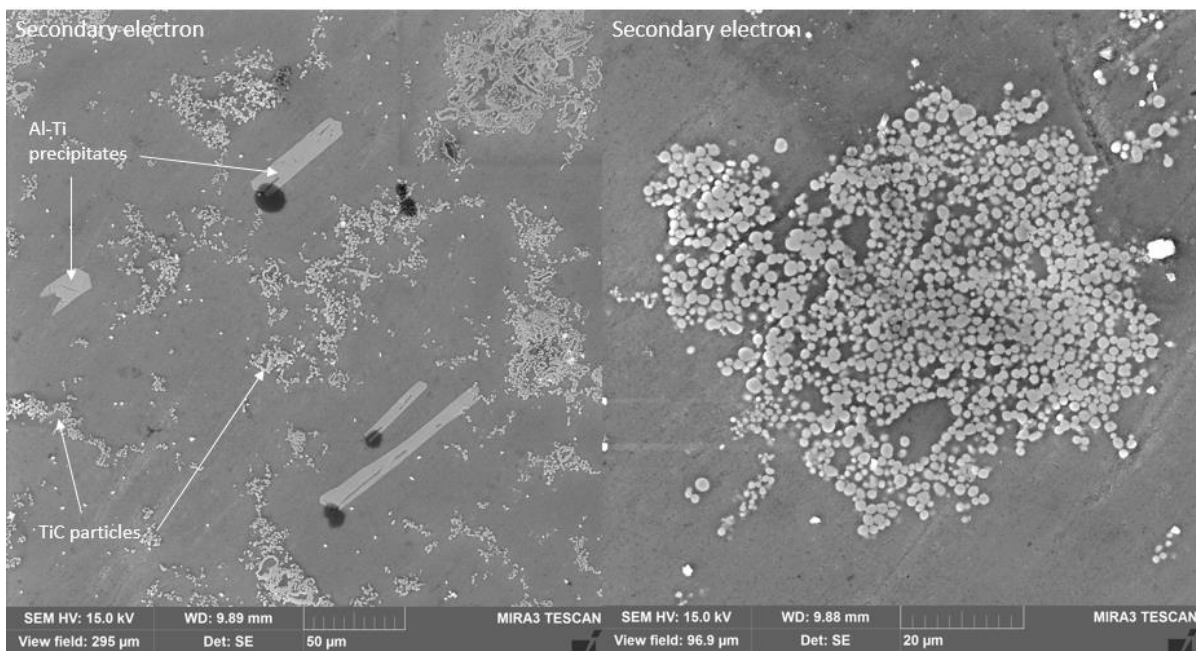


Figure 31: SEM micrograph of experiment 2, polished surface.

When diluted into A356 and gravity cast, the particles were found to be mostly clustered inside of alumina precipitates. Tensile bars from this experiment did not result in significant strengthening, though there were TiC particles seen at some parts of the fracture surface.

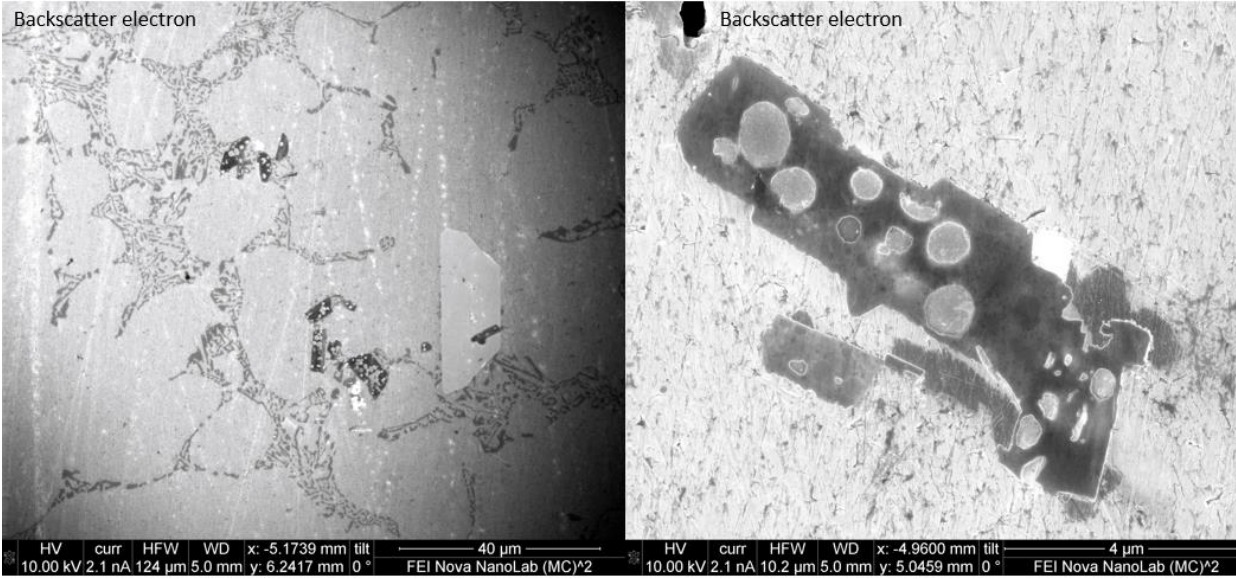


Figure 32: experiment 2 material, polished surface, after dilution in A356, ~1:4 ratio

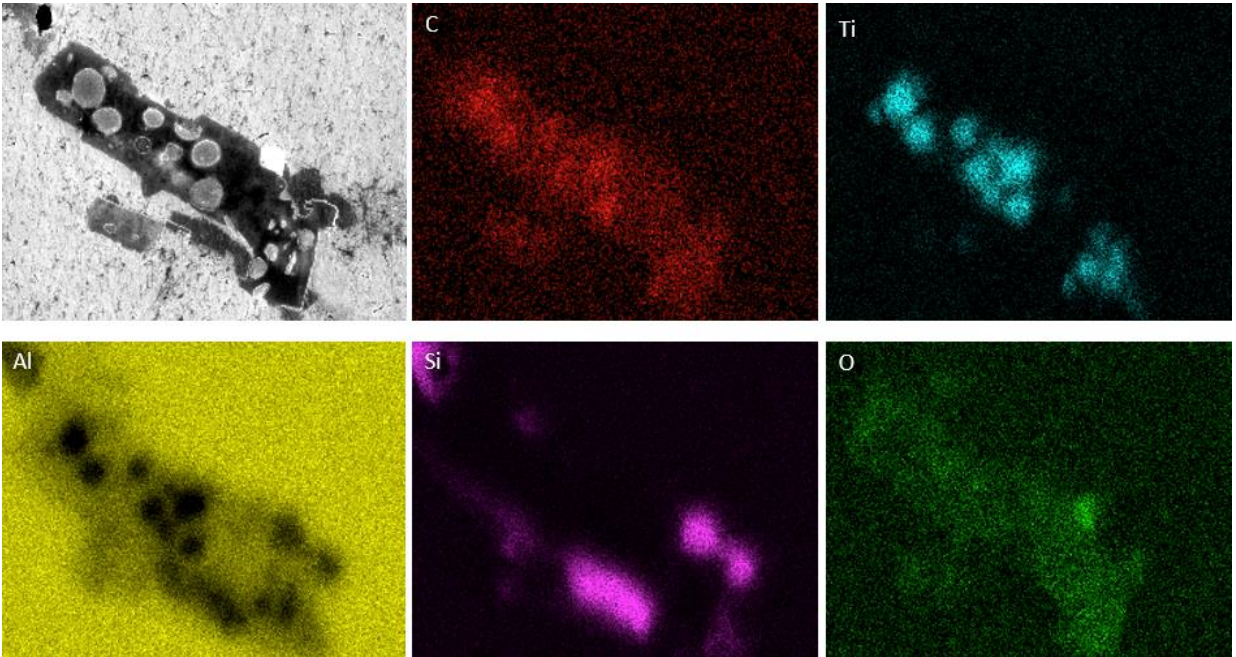


Figure 33: EDS maps of diluted material from SHS experiment 2

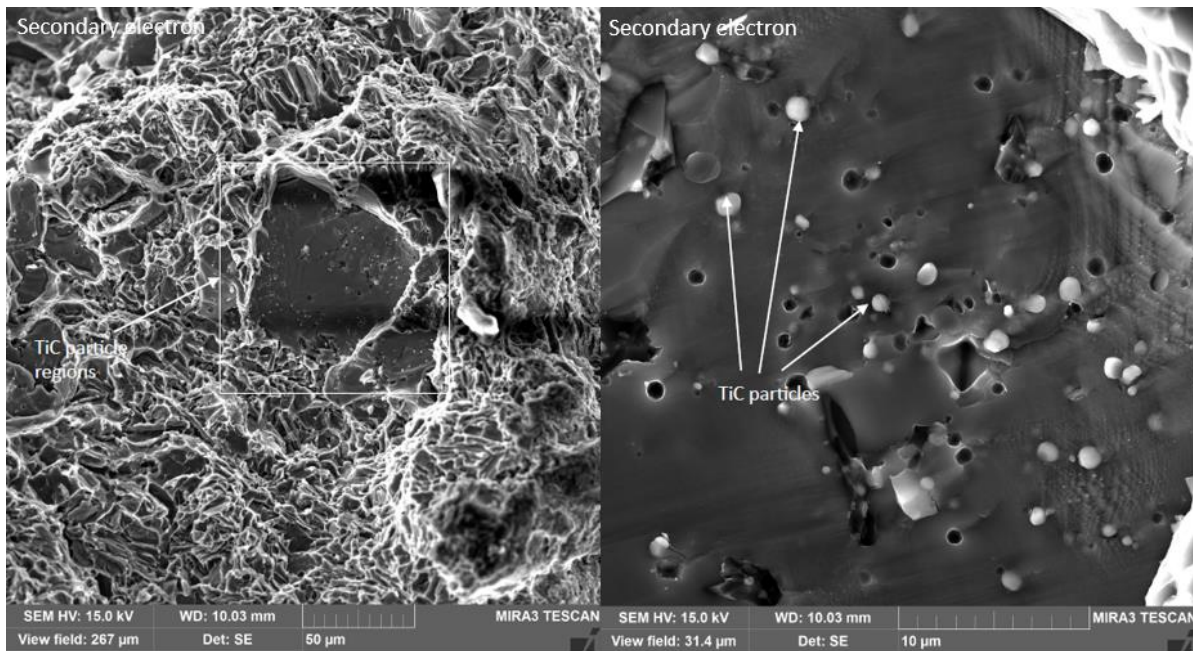


Figure 34: SEM fracture surface of experiment 2 after dilution in A356

Experiments 3-8: Variation of mixing method and composition

Averaging all these experiments, temperatures were measured at $842.5 \pm 17.5^\circ\text{C}$. It is possible these pellets would have reacted at slightly lower temperatures given enough time, but in this range, pellets took between 16-40 seconds to ignite. Generally, for these and future experiments, temperature was adjusted after the first several pellets reacted, such that ignition would occur within 20 seconds.

The microstructures of these were fairly similar to that of experiment 2, except with highly variable APS between batches. The comparison between this set as well as experiment 2 is shown in Figure 35.

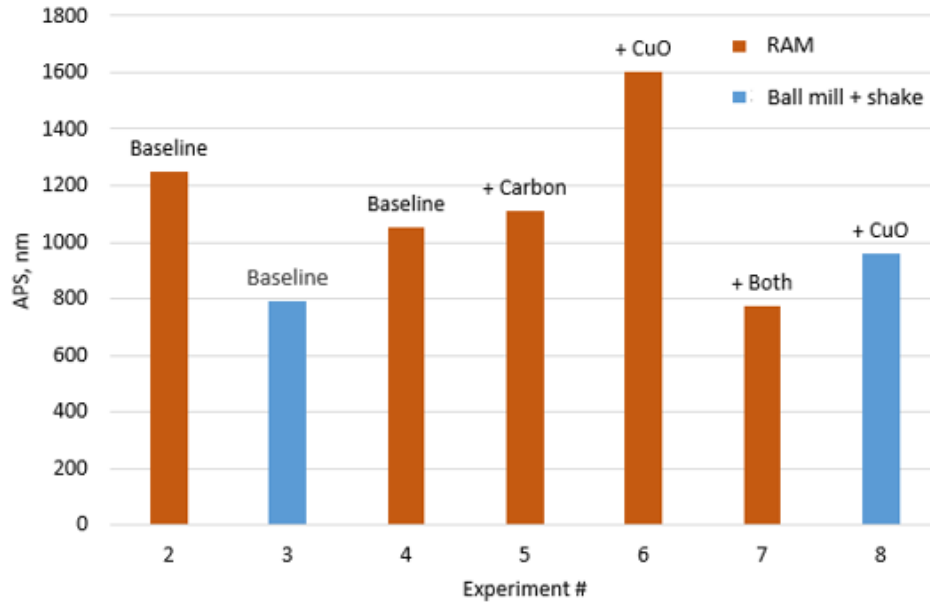


Figure 35: APS of experiments 2-8

Experiment 9: Initial use of intermediate size Ti powder

Smaller Ti powder clearly made a difference in time to ignition as well as minimum reaction temperature, with pellets igniting after 4-8 seconds at $822.5 \pm 27.5^\circ\text{C}$. APS was 699nm.

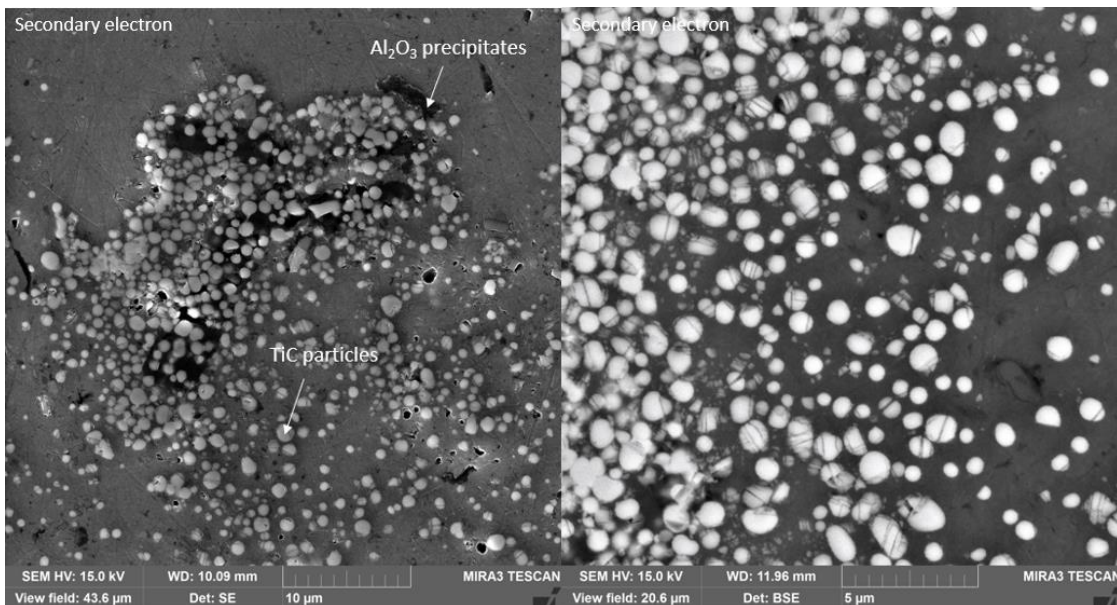


Figure 36: SEM micrograph of experiment 9

Experiments 10 & 11: Loose powder reactions using large packets

Experiment 10 and 11, done at Eck in Al-Mg alloy and WPI in pure Al respectively, both formed a smaller fraction of TiC than other batches due to the scattering of unreacted powder.

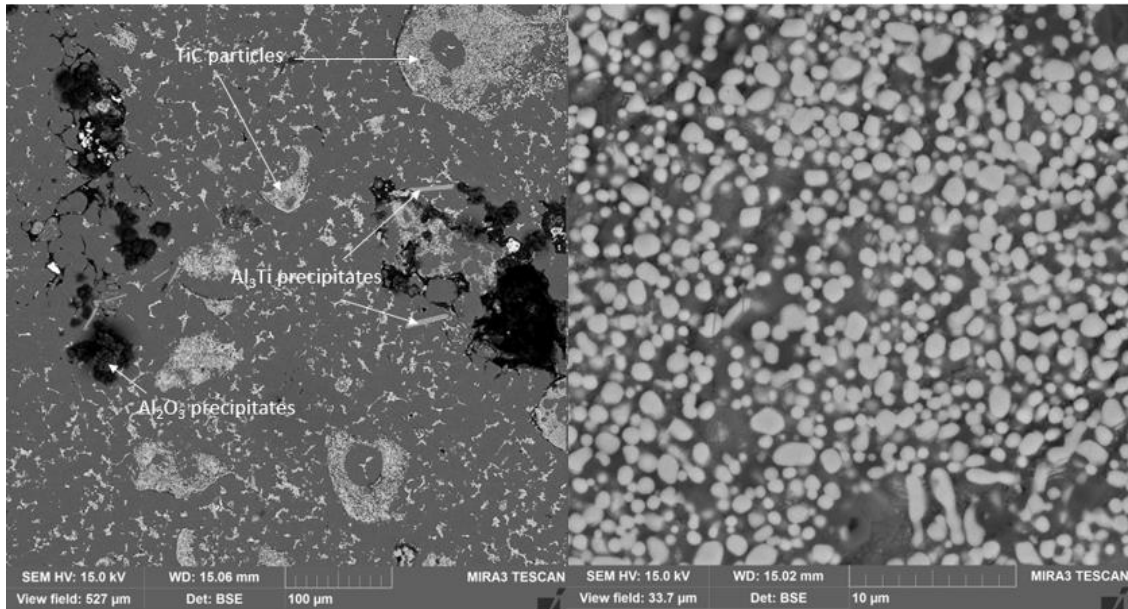


Figure 37: SEM micrograph of experiment 10.

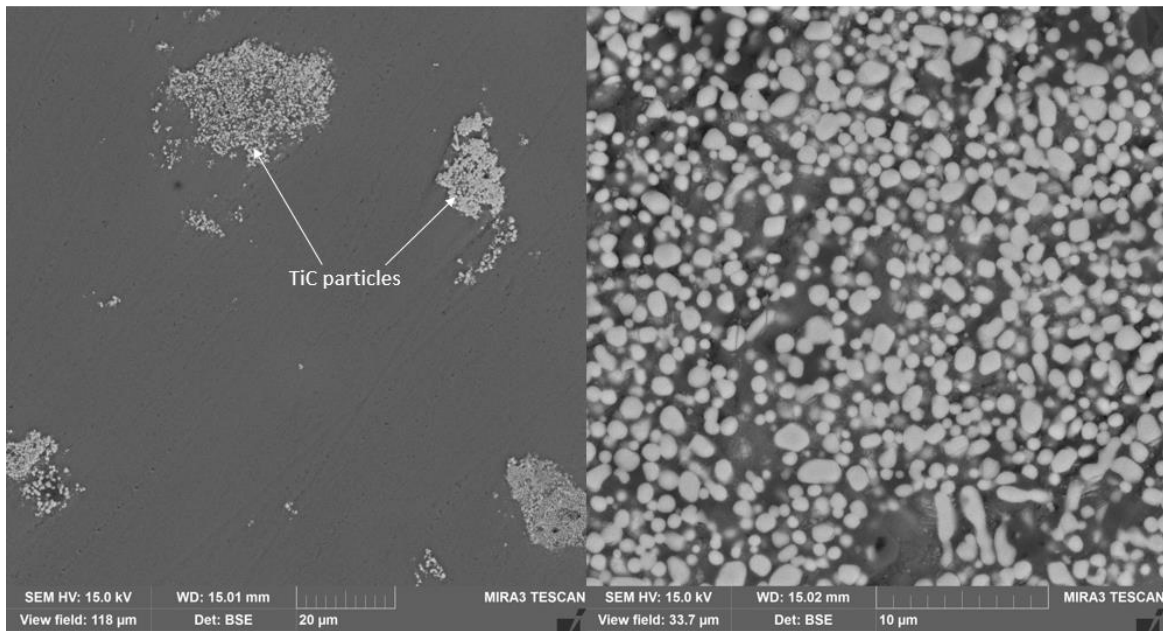


Figure 38: SEM micrograph of experiment 11.

These did demonstrate that a very similar reaction would result from igniting loose powder. Experiment 11 had lower particle size and very few extraneous phases, as well as a smaller APS at 579nm versus 857nm in experiment 10.

Experiments 12 & 13: WPI vs. Eck batches in Al-Mg, and Squeeze-cast plates

Experiment 12 resulted in the smallest APS of the densely-packed pellets, at 655nm. Experiment 13, the reaction of pellets in a slightly larger melt along with ultrasonic was not as successful as the smaller-scale reaction, with TiC found almost exclusively attached to oxides. Precipitates with Al and carbon EDS signals were seen, which was not present in any of the earlier experiments. These are assumed to be Al_4C_3 . Besides ultrasonic processing, the differences between these reactions are that experiment 13 pellets were not heated in a 100°C oven before reacting and may have had a longer dwell time in the melt before being cast.

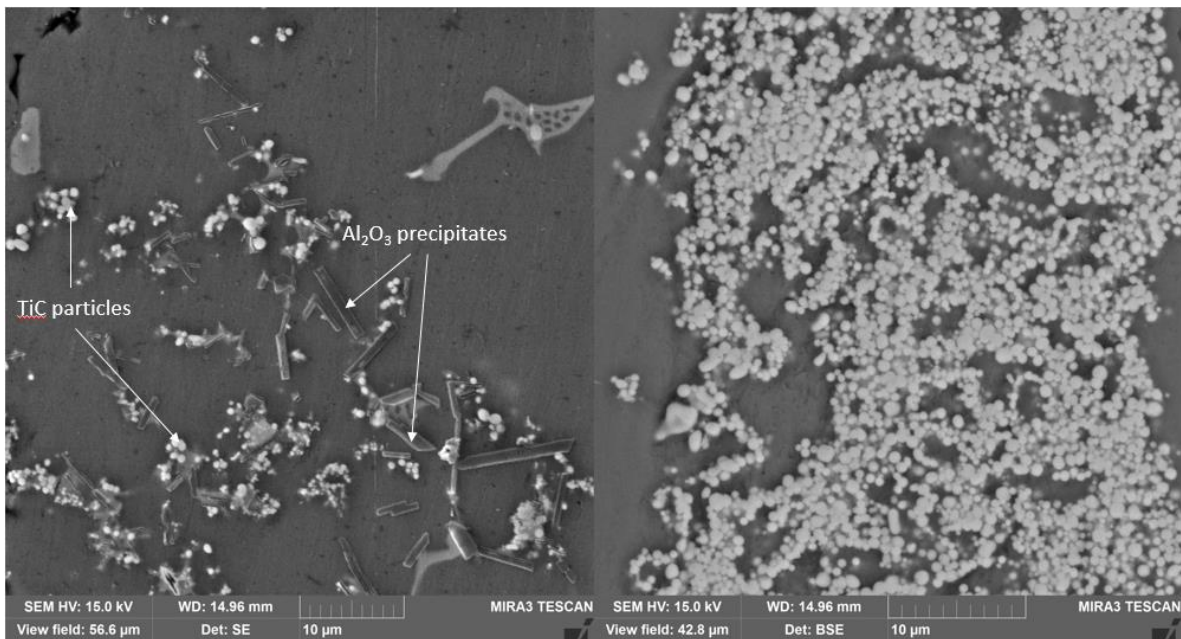


Figure 39: SEM micrograph of experiment 12

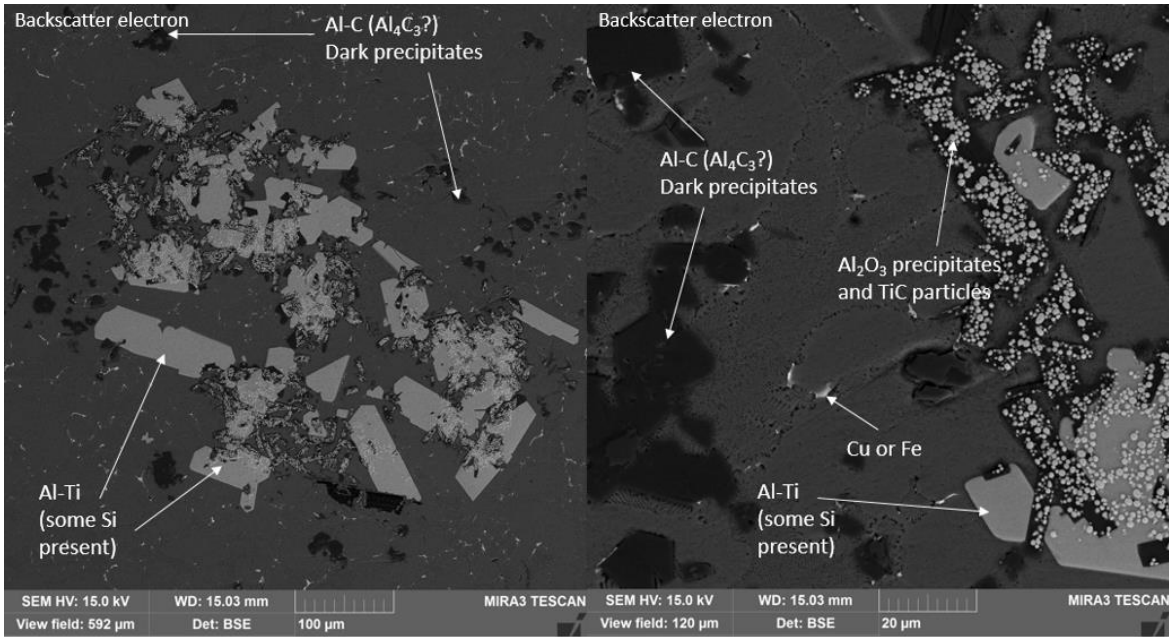


Figure 40: SEM micrograph of experiment 13

Experiments 14 and 15: smaller foil packets

Experiment 14 material was not characterized, due to the reacted packets not being possible to stir into the matrix. Experiment 15 material had the smallest APS out of all the experiments that had mostly complete reactions, at 495nm. Analysis was done at several locations of the material, as well as one sample which was not well-mixed.

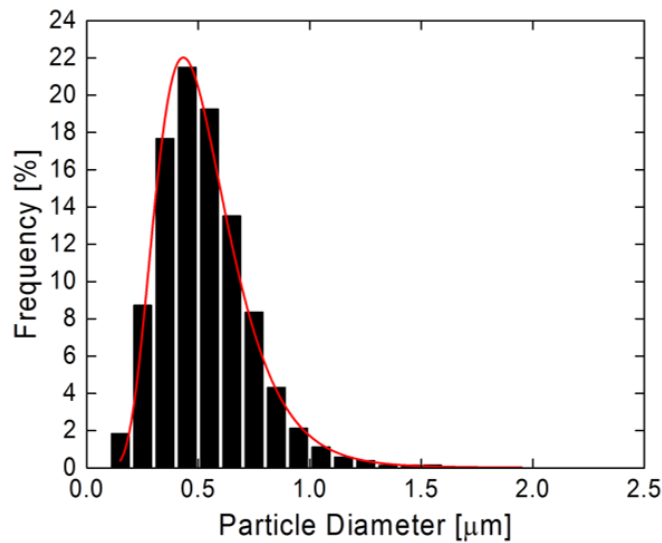


Figure 41: particle size distribution of experiment 15.

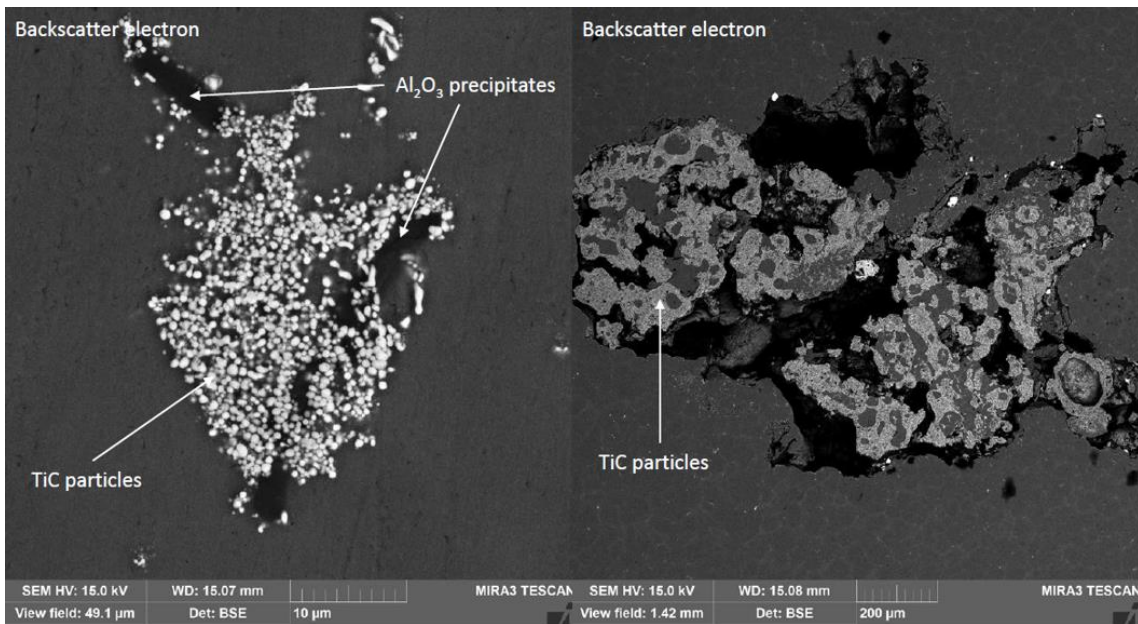


Figure 42: SEM micrograph of experiment 15, with porosity occurring on the right.

Experiment 16: broken pellets

Material from experiment 16 shows some unreacted carbon as well as a small amount of alumina, though Al₃Ti is not present. APS was 660nm.

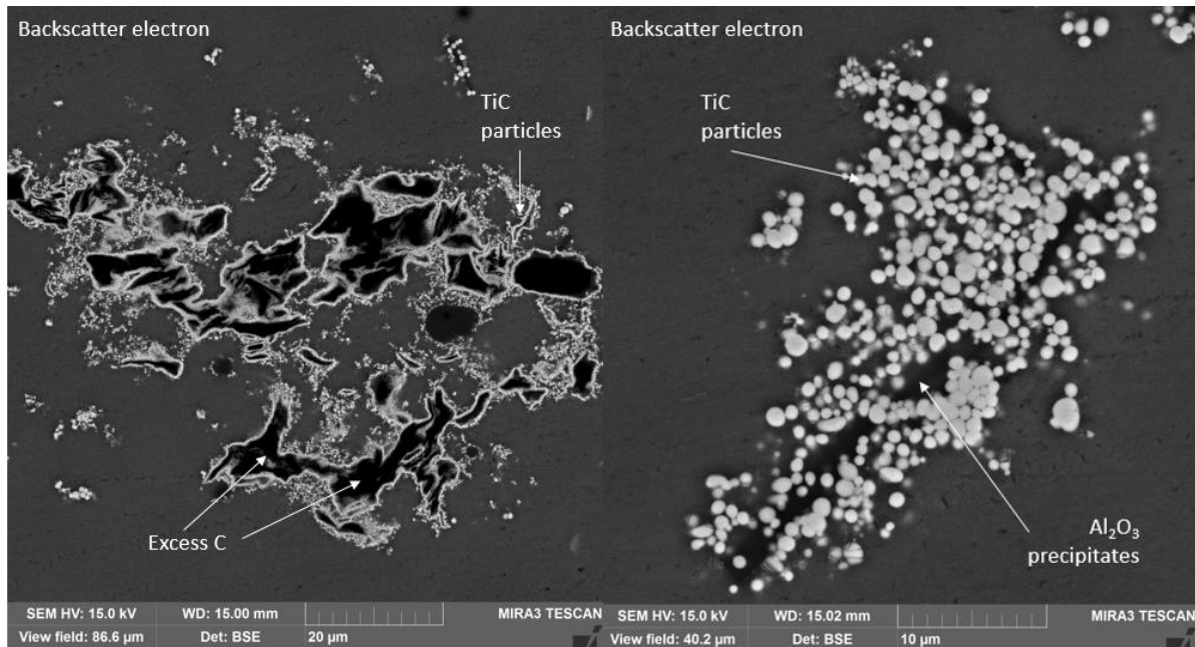


Figure 43: SEM micrograph of experiment 16.

Experiment 17: ignition from one end of pellet

In experiment 17, The presence of large amounts of unreacted carbon as well as Al_3Ti with TiC particles in close proximity shows an intermediate stage in the reaction. During the reaction, most of the reacting region must have lost too much heat to the surrounding Al to progress to completion. This material had a highly variable structure, with another location containing larger particles which were around 500nm, likely corresponding to the end of the pellet which contained CuO.

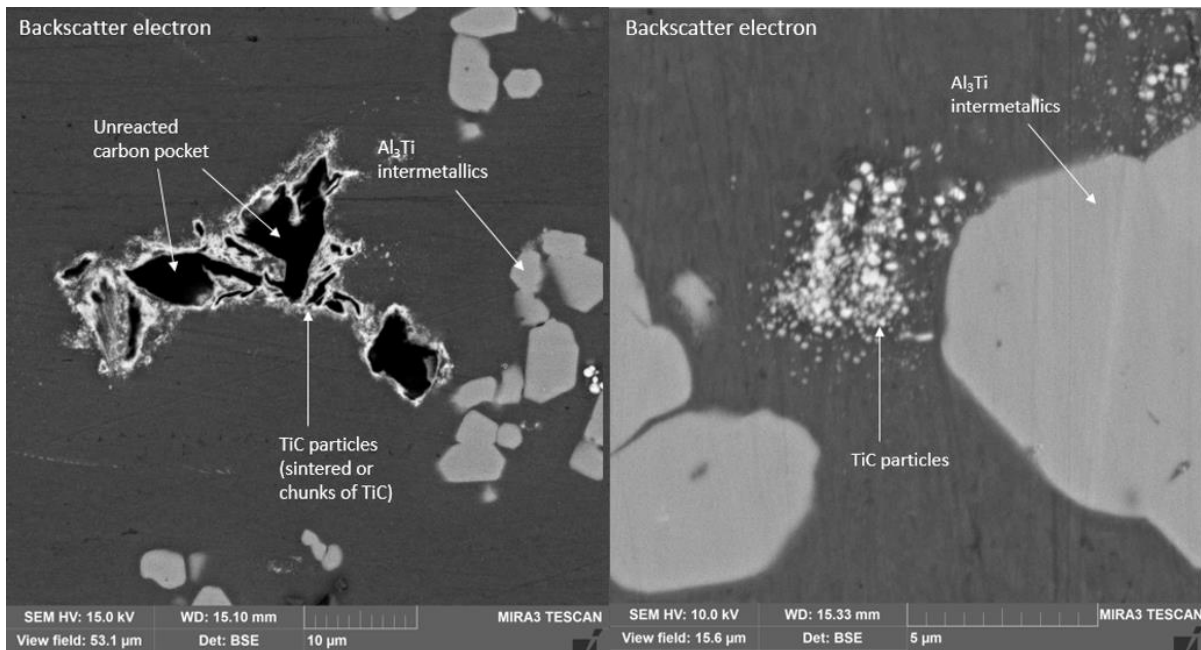


Figure 44: SEM micrograph of experiment 17.

Experiment 18: Squeeze-cast plates from direct reaction: comparison of pure Al, Al-Mg and Al-Mg-Ni

Experiment 18a, which contained P1020 reinforced with ~2vol% TiC, resulted in the most successful ultrasonic SHS results to date. As can be seen in Figure 45, mixing and particle capture on solidification are still not ideal, since some large clusters were observed as well as inter-granular clusters. Many TiC particles were also successfully engulfed into grains as well.

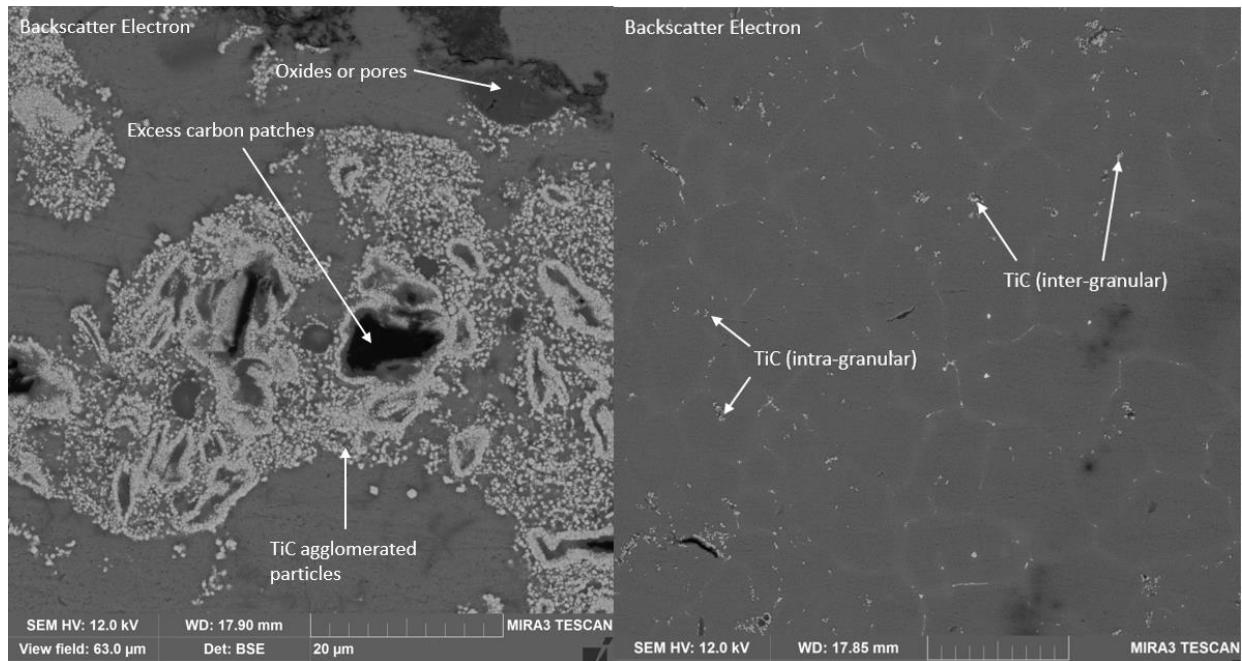


Figure 45: SEM micrograph of experiment 18a, polished surface.

Fracture surfaces are shown in Figures 45 and 46, with some TiC appearing within ductile fracture cup formations. The fracture occurred at a large pore in this particular bar. Averaged with four stronger bars, the results were still impressive. Tensile test results of plain P1020 as well as 18a and 18b reinforced material are listed in Table 4. At the time of writing, SEM analysis of 18b and 18c were still in progress. The 18c batch did not have enough metal to cast into a full plate for tensile testing.

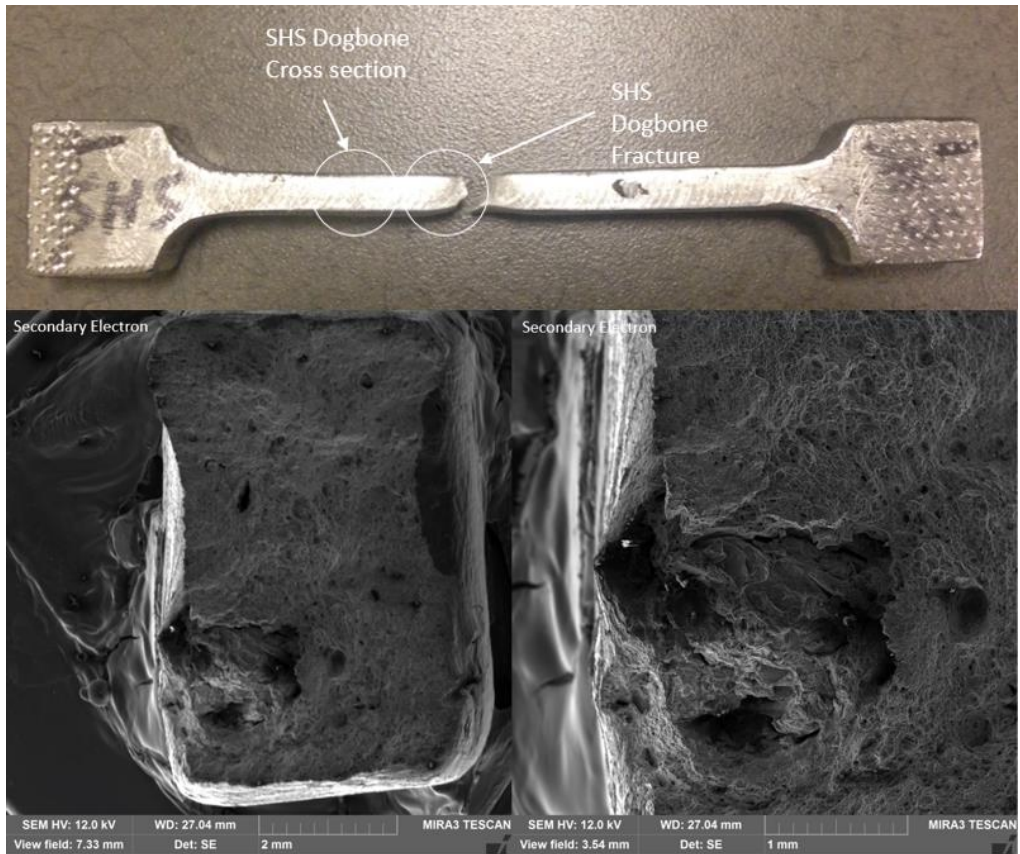


Figure 46: tensile dog bone and SEM fracture surface of SHS experiment 18a.

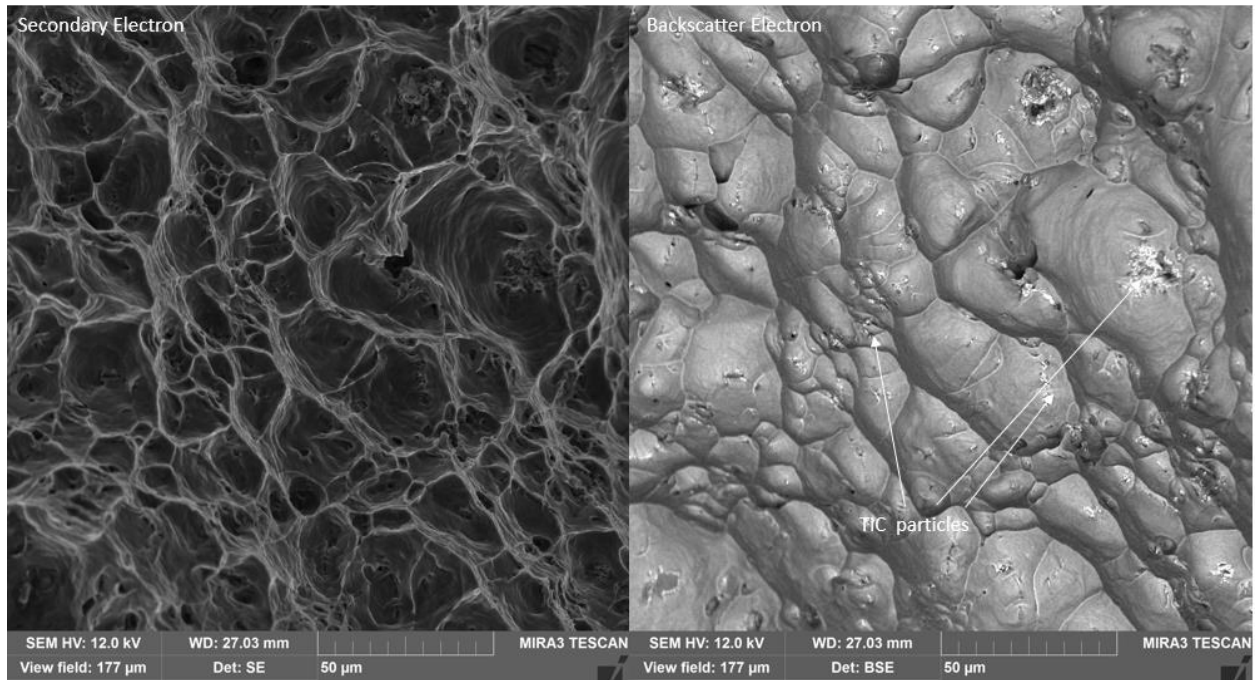


Figure 47: SEM fracture surface of SHS experiment 18a.

Table 4: tensile tests of P1020 unreinforced versus reinforced with ~2vol% TiC. The material from 18b contained 1.99wt% Mg after processing, as well as 0.785wt% Cu and 1.88wt% Ti.

Tensile bars at RT:	P1020 (>99.7wt%Al)	(18a) P1020 + TiC	(18b) P1020 + Mg + TiC- sample 1	(18b) P1020 + Mg + TiC- sample 2
Tensile strength, ksi	8.7	13.4	19.0	19.2
Yield stress, ksi	4.6	6.2	15.6	Not reliable- hardware malfunction
Elongation, %	26.2	21.0	2.4	4.9

Average melt temperatures and particle sizes are shown in Figure 48 for a few of the experiments having different pellet types.

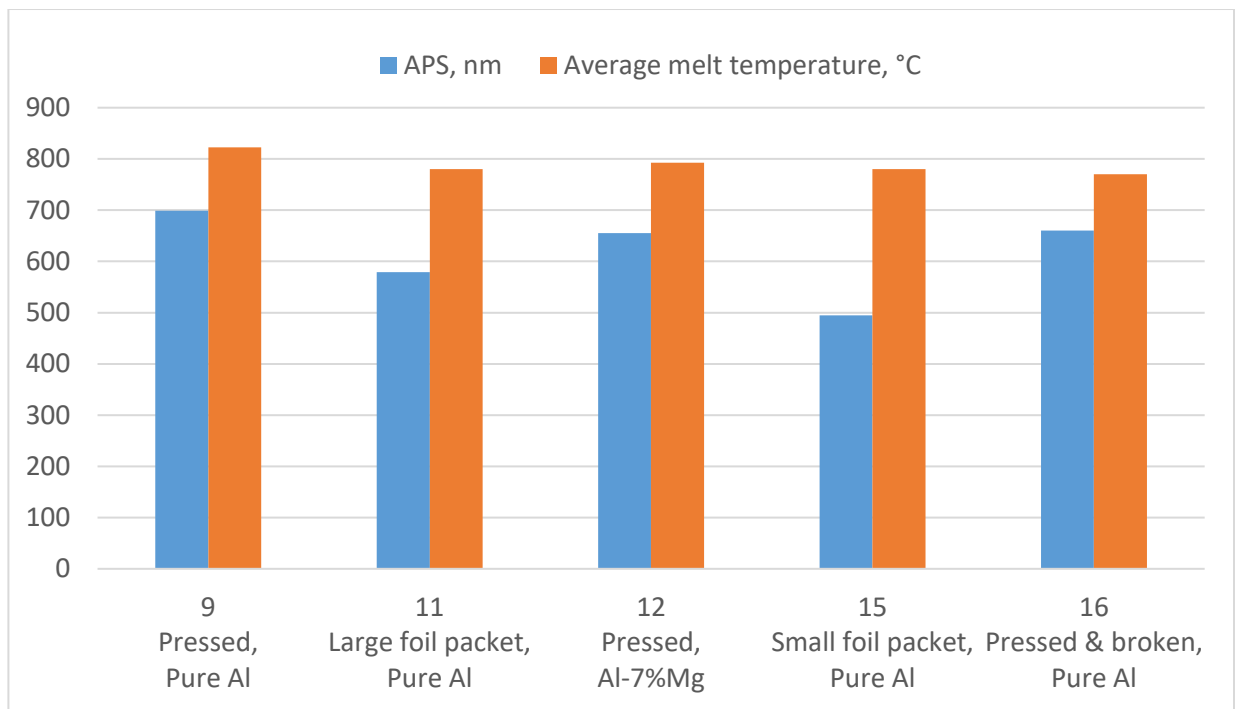


Figure 48: comparison of APS and melt temperatures during reaction for experiments with different pellet types

All of these contained the same powder composition except 11, which contained nano-sized carbon. Despite the smaller carbon, the large foil packet still produced larger particles.

3.2.2 Discussion

Particle size

The wide variety of factors modified throughout these experiments and the small sample size makes it difficult to draw many conclusions. However, some valuable observations stand out. For example, loose powder packets allow the particle size to decrease slightly vs. compact pellets. The lower density and ability to quickly react in lower temperatures likely makes the peak reaction temperature, and therefore particle size, decrease. The disadvantage is that these packets take longer to prepare and add to the melt and tend to form more oxides. Breaking pressed pellets was expected to decrease the particle size because the center of the pellet would not heat up and cause larger particle growth than the edges. This did not turn out to be a significant factor.

Experiment 17 (Figure 44) is interesting because it shows the patterns of TiC nucleation around both Ti and carbon particles, during an intermediate stage in the reaction, as well as the minimum TiC size that will likely be possible for the current reactant sizes. It is possible the Al or CuO levels could be modified further to decrease this minimum, or the Ti and carbon particle size decreased, but any reduction in size of Ti powder would also raise the cost of the process. Reducing Ti size seemed to have more of an impact on TiC APS than reducing carbon size, and though experiments using a larger variety of particle sizes could confirm this.

Particle dispersion and mechanical properties

It was clear that A356 was not a useful matrix to react directly in, and even when reacted in pure Al and diluted in A356, particles were for the most part not showing good dispersion except for in one area seen in the fracture surface (Figure 32 & Figure 34).

The earlier tensile tests were unsuccessful due to the significant particle clustering observed, and in the case of experiment 2 (Figure 34), the A356 matrix may have limited the matrix-particle bond strength. The particle dispersion in experiment 18a (Figure 45) is not perfect but is encouraging, since some TiC was found within grains and none was attached to alumina as in experiment 13. It

seems likely that an Al-Mg alloy would be a good choice for producing cast components, though it remains to be seen if the SHS material maintains a good bond with the matrix even after temperature cycling.

As for improving TiC dispersion with ultrasonic processing, Tzanakis et al. reported that efficient processing requires fluid to pass through the cavitation zone which is beneath the probe tip. For a continuous flow process, they found acoustic pressures to be an order of magnitude higher than 7.5cm upstream and downstream of the probe⁴¹. For a stationary crucible process, dispersion may improve if mixing is aided using high gas flow through the probe and/or an impeller. Also, recent work from OSU has suggested that additions of Ni improve particle engulfment into grains during directional solidification, because of the viscosity effect of this alloying element.⁴² More of this type of work is planned for the SHS composites.

Ensuring complete reactions

Driving the reaction to completion is clearly an issue, as Al_3Ti or unreacted carbon often remain in the SHS material. In most experiments, Al_3Ti remained when unreacted carbon did not, but in the case of experiment 18a, the reverse was seen, so the control of these precipitates is not fully understood. To help understand the Al_3Ti dissolution that must occur to allow for TiC nucleation, collaborators at the Ohio State University performed a DICTRA simulation, as seen in Figure 49 & Figure 50.⁴² The Al_3Ti particle was assumed to initially have a 20 μm diameter, then dissolution of the particle in Al at a few temperatures in the expected range for SHS was simulated. In order to fully dissolve the particle, the minimum reaction temperature is somewhere between 1200° and 1300°. This is a reasonable range considering the reactions observed by Cho et al., in which a maximum temperature of for melt temperature of 750° was 1318.8°C.¹⁵ That pellet did not react fully except in the center where the temperature was measured, and the edges could experience lower peaks due to heat transfer to the surrounding melt. In addition to more simulations for different sizes of Ti powders as well as for the dissolution and reaction of carbon particles, knowledge could be gained from heat transfer simulations using pellets and foil packets of various sizes and densities. It could also be worthwhile exploring an alternative to compact shapes: extending and narrowing the foil package would result in a cored wire with negligible temperature differences between the center and edges.

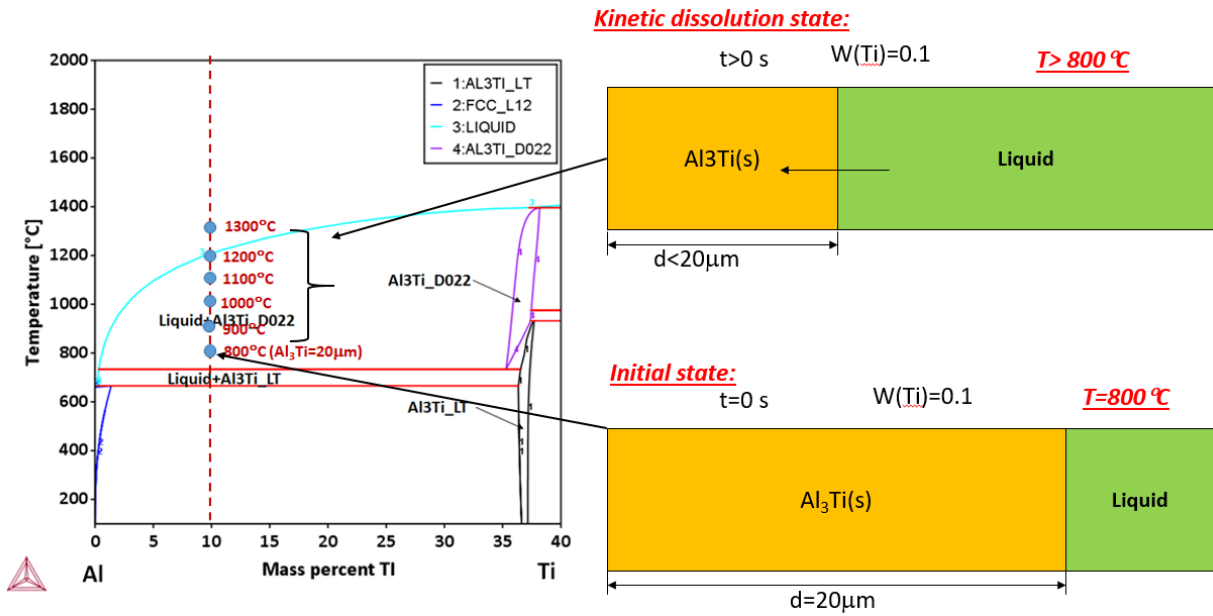


Figure 49: Al₃Ti dissolution simulation in relation to the Al-Ti phase diagram

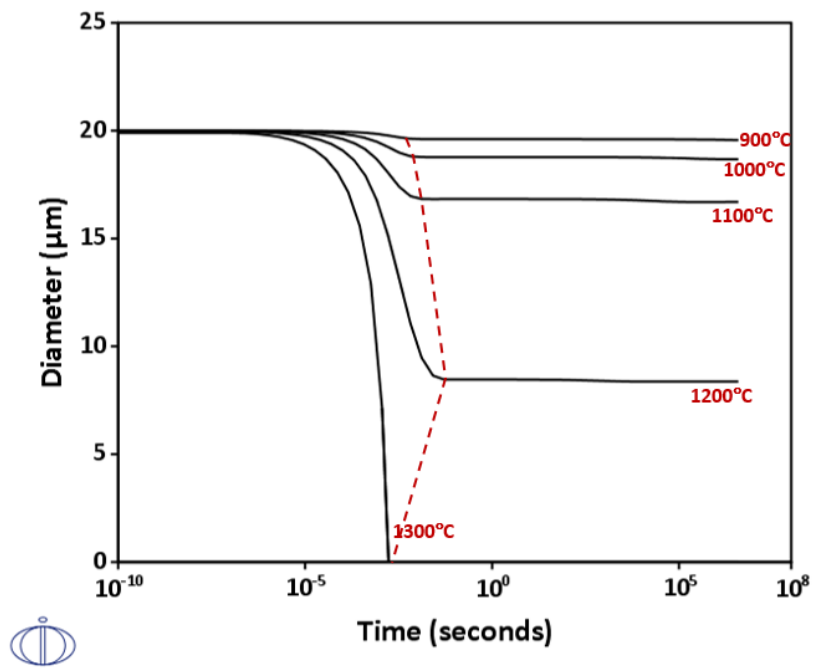


Figure 50: Simulation of Al₃Ti particle dissolution

4 Recommendations for future work

4.1 ISGR

Though serious roadblocks limited the number of experiments that could be done in this work, a robust system has been demonstrated at a scale which can produce up to 20lbs batches, and the manufacturability of components has been improved. Improving the particle size distribution and cleanliness of the process is critical, and the following are some key recommendations for ISGR:

- Carefully evaluate what information can be gained from cold fluid models, simulations etc. in order to possibly save time on experimentation and design modifications. Collaboration with a fluid mechanics expert could be beneficial.
- Modify the process to reduce the extraneous reactions on the ingot surface. Maintaining a large-scale system under a highly-pure inert atmosphere could be inconvenient, but possibly a flux cover could be added.
- Revisit ammonia or attempt the reaction with a nitrogen-hydrogen mix, since this could allow for reduction or removal of lithium from the process if particle growth can be controlled properly.
- Eventually develop a system which can allow composite master alloy to flow or be ladled out of the ISGR system and cooled under protected atmosphere or immediately diluted. Waiting for the ingot to cool in the furnace is an inconvenience for lab research, but a deal-breaker for commercial production.

4.2 SHS

The TiC SHS process is more promising in the short term has been limited to mostly submicron-sized particles, but the tensile properties at room temperature are impressive even with significant porosity and imperfect particle dispersion. The following are some key recommendations for SHS:

- Verify that the SHS material with the current particle size can improve material properties significantly at elevated temperatures, including fatigue and creep testing with observation of how well the particles remain bonded to the matrix over time.
- Explore aluminum-wrapped powder methods further, to continue decreasing particle size. Preliminary experiments showed incomplete reactions, but a cored wire process and further adjustment of reactant ratios and particle sizes could be worth attempting.
- Revisit TiO₂-based composites which were developed by researchers at CSM. These could be attempted as in-situ experiments to produce low vol% composites and compared apples-to-apples with Ti-based SHS material.
- Figure out the ideal temperature range and maximum holding time needed to prevent undesirable phases to form in large batches. If Mg is proven to encourage formation of these phases, it could be stirred in quickly when the melt is at casting temperature, then immediately cast.

5 References

1. Lee, J. A. Commercialization of NASA's High Strength Cast Aluminum Alloy for High Temperature Applications. in *28th Annual Conference on Composites, Materials & Structures* (USACA, 2004).
2. Weiss, D. Development and Casting of High Cerium Content Aluminum Alloys. *Mod. Cast.* 35–38 (2017).
3. Lee, J. A. Cast Aluminum for High Temperature Applications. in *Automotive Alloys 2003 in The 132nd TMS Annual Meeting & Exhibition 2–6* (TMS, 2003).
4. Weiss, D. Personal correspondence. (2018).
5. Garrett, W. *et al.* Die Castable Aluminum Metal Matrix Composites by Self-propagating High-temperature Synthesis. in *Die Casting Congress & Tabletop* (2011).
6. Poirier, D., Drew, R. A. L., Trudeau, M. L. & Gauvin, R. Fabrication and properties of mechanically milled alumina/aluminum nanocomposites. *Mater. Sci. Eng. A* **527**, 7605–7614 (2010).
7. Borgonovo, C. Synthesis of Aluminum-Aluminum Nitride Nanocomposites by Gas-Liquid Reactions. (Worcester Polytechnic Institute, 2013).
8. Furukawa, M., Horita, Z., Nemoto, M. & Langdon, T. G. Review Processing of metals by equal-channel angular pressing. *J. Mater. Sci.* **36**, 2835–2843 (2001).
9. Xiaodan, L., Yuchun, Z., Feng, Q. & Haixi, Z. Preparation of Metal Matrix Composites Reinforced with Nano-SiC Particles by Stir Casting Technique. in *Proc.139th Annual Meeting and Exhibition TMS* (2010).
10. Li, X., Yang, Y., Weiss, D. . Ultrasonic Cavitation Based Dispersion of Nanoparticles in Aluminum Melts for Solidification Processing of Bulk Aluminum Matrix Nanocomposite: Theoretical Study, Fabrication and Characterization. *Trans. Am. Foundry Soc.* **115**, 249–260 (2007).
11. Liu, W., Cao, C., Xu, J., Wang, X. & Li, X. Molten salt assisted solidification nanoprocessing of Al-TiC nanocomposites. *Mater. Lett.* **185**, 392–395 (2016).
12. Mula, S., Padhi, P., Panigrahi, S. C., Pabi, S. K. & Ghosh, S. On structure and mechanical properties of ultrasonically cast Al-2% Al₂O₃nanocomposite. *Mater. Res. Bull.* **44**, 1154–1160 (2009).
13. Anza, I., Borgonovo, C., Makhlof, M. The Rotating Impeller Gas-Liquid In-situ Method for Aluminum Matrix Nano-composites manufacturing.
14. Merzhanov, A. G. & Borovinskaya, I. P. Self-spreading high-temperature synthesis of refractory inorganic compounds. *Dokl. Akad. Nauk SSSR, Seriya Khimiya* **204**, 366–369 (1972).
15. Cho, Y. H., Lee, J. M. & Kim, S. H. Al-TiC Composites Fabricated by a Thermally Activated Reaction Process in an Al Melt Using Al-Ti-C-CuO Powder Mixtures. Part I: Microstructural Evolution and Reaction Mechanism. *Metall. Mater. Trans. A* **45**, 5667–

- 5678 (2014).
16. Nuechterlein, J. Production of Ceramic Nanoparticles Through Self-Propagating High-Temperature Synthesis (SHS) and Their Introduction Into a Metallic Matrix to Form Metal Matrix Composites (MMC). (Colorado School of Mines, 2013).
 17. Zhang, Z. & Chen, D. L. Consideration of Orowan strengthening effect in particulate-reinforced metal matrix nanocomposites: A model for predicting their yield strength. *Scr. Mater.* **54**, 1321–1326 (2006).
 18. Yang, H. *et al.* Microstructure and mechanical properties at both room and high temperature of in-situ TiC reinforced Al–4.5Cu matrix nanocomposite. *J. Alloys Compd.* **767**, 606–616 (2018).
 19. Deng, K. *et al.* Microstructure and strengthening mechanism of bimodal size particle reinforced magnesium matrix composite. *Compos. Part A Appl. Sci. Manuf.* **43**, 1280–1284 (2012).
 20. Cho, Y. H., Lee, J. M. & Kim, S. H. Al-TiC Composites Fabricated by a Thermally Activated Reaction Process in an Al Melt Using Al-Ti-C-CuO Powder Mixtures: Part II. Microstructure Control and Mechanical Properties. *Metall. Mater. Trans. A Phys. Metall. Mater. Sci.* **46**, 1374–1384 (2015).
 21. Rong, P., Zhou, H. P., Ning, X. S., Lin, Y. B. & Wei, X. The study and fabrication of Al/AlN substrate. *Mater. Lett.* **56**, 465–470 (2002).
 22. Xu, J. Q., Chen, L. Y., Choi, H. & Li, X. C. Theoretical study and pathways for nanoparticle capture during solidification of metal melt. *J. Phys. Condens. Matter* **24**, (2012).
 23. Daniel, B. S. S. & Murthy, V. S. R. Directed melt oxidation and nitridation of aluminium alloys: a comparison. *Mater. Des.* **16**, 155–161 (1995).
 24. Scholz, H. . & Greil, P. Nitridation reactions of molten Al-(Mg, Si) alloys. *J. Mater. Sci.* **26**, 669–677 (1991).
 25. Borgonovo, C. & Makhlof, M. M. Synthesis of Aluminum–Aluminum Nitride Nanocomposites by a Gas–Liquid Reaction II. Microstructure and Mechanical Properties. *Metall. Mater. Trans. A Phys. Metall. Mater. Sci.* **47**, 1818–1827 (2016).
 26. Borgonovo, C. & Makhlof, M. M. Synthesis of Aluminum-Aluminum Nitride Nanocomposites by Gas-Liquid Reactions I. Thermodynamic and Kinetic Considerations. *Metall. Mater. Trans. A Phys. Metall. Mater. Sci.* **47**, 5125–5135 (2016).
 27. Anza, I. & Makhlof, M. M. Synthesis of Aluminum-Titanium Carbide Micro and Nanocomposites by the Rotating Impeller In-Situ Gas–Liquid Reaction Method. *Metall. Mater. Trans. B Process Metall. Mater. Process. Sci.* **49**, 466–480 (2017).
 28. Anza, I. Synthesis of Aluminum-Titanium Carbide Micro and Nanocomposites by the Rotating Impeller In-Situ Gas–Liquid Reaction Method. (Worcester Polytechnic Institute, 2016). doi:10.1007/s11663-017-1148-9

29. Tatterson, G. B. *Fluid Mixing and Gas Dispersion in Agitated Tanks*. (McGraw-Hill, 1991).
30. Oldshue, J. Y. *Fluid Mixing Technology*. (McGraw-Hill, 1983).
31. Okamoto, Y., Nishikawa, M., Hashimoto, K. Energy dissipation rate distribution in mixing vessels and its effects on liquid-liquid dispersion and solid-liquid mass transfer. *Int. Chem. Eng.* **21**, 88–91 (1981).
32. Garrett, W. Control of Self-Propagating High-Temperature Synthesis Derived Aluminum-Titanium Carbide Metal Matrix Composites. (Colorado School of Mines, 2012).
33. Udvardy, S., Makhlof, M. M. & Nuechterlein, J. Development of High Performance Nano-Composite Materials. in *Die Casting Congress & Exposition* (NADCA, 2012).
34. Rajan, T. P. D., Pillai, R. M. & Pai, B. C. Reinforcement coatings and interfaces in aluminium metal matrix composites. *J. Mater. Sci.* **33**, 3491–3503 (1998).
35. Segur, J. . & Oberstar, H. Viscosity of Glycerol and Its Aqueous Solutions. *Ind. Eng. Chem.* **43**, 2117–2120 (1951).
36. Dinsdale, A. & Quedsted, P. The viscosity of aluminium and its alloys — A review of data and models. *J. Mater. Sci.* **39**, 7221–7228 (2004).
37. Reese, C., Gladstein, A., Liu, X. & Taub, A. Unpublished work from UM.
38. Contreras, A., León, C. A., Drew, R. A. L. & Bedolla, E. Wettability and spreading kinetics of Al and Mg on TiC. *Scr. Mater.* **48**, 1625–1630 (2003).
39. Mueller, S., Llewellyn, E. W. & Mader, H. M. The effect of particle shape on suspension viscosity and implications for magmatic flows. *Geophys. Res. Lett.* **38**, 1–5 (2011).
40. Yu, W., Xie, H., Li, Y. & Chen, L. Experimental investigation on thermal conductivity and viscosity of aluminum nitride nanofluid. *Particuology* **9**, 187–191 (2011).
41. Tzanakis, I., Lebon, G. S. B., Eskin, D. G. & Pericleous, K. Optimization of the Ultrasonic Processing in a Melt Flow. *Light Met.* **2016** 833–836 (2016).
doi:10.1002/9781119274780.ch141
42. Shi, R., Meier, J. & Luo, A. Unpublished work from OSU. (2018).